Available online at www.sciencedirect.com

ScienceDirect

Underground Space 25 (2025) 239–261

www.keaipublishing.com/undsp

Research Paper

Biaxial compression behavior and stability analysis of wedge blocks in tunnel sidewalls: Experimental investigation and support effect evaluation

Ruiyang Bi, Minghui Liu, Jian Zhou, Kun Du *

School of Resources and Safety Engineering, Central South University, Changsha 410083, China

Received 12 March 2025; received in revised form 7 May 2025; accepted 16 May 2025
Available online 24 September 2025

Abstract

In complex jointed rock masses, wedge blocks are likely to form on the tunnel sidewalls after excavation, and the mechanical properties and stress environment of the surrounding rock have a significant impact on their stability. In this study, cubic rock specimens with prefabricated wedge blocks and arched tunnel features were tested under biaxial compression. Acoustic emission (AE) and digital image correlation technologies were used to monitor crack propagation and specimen failure in real-time. The results showed that supported specimens exhibited higher strength during both the peak and post-peak stages, with a slower strength decline after the peak. The support regulated AE hit rates and enhanced energy storage capacity. Different specimens displayed varying strain evolution, with supported specimens generally having higher lateral strain than shear strain. In unsupported specimens, tensile and shear stresses were concentrated at the wedge block apex, while supported specimens showed more complex stress variations, especially under the influence of wedge blocks. Stable specimens experienced shear sliding failure, while extremely stable specimens experienced both shear sliding and tensile fracture. As horizontal stress (σ_3) increased, specimen strength and wedge block failure both increased. Triangular wedge blocks played a decisive role in tunnel stability, with extremely stable triangular blocks providing greater safety. In addition, a typical stability analysis method for wedge blocks was proposed. The findings provide a scientific basis for rock mass stability assessment and support measure selection in tunnel design.

Keywords: Underground mining; Wedge blocks; Biaxial compression; Discrete element simulation; Tunnel stability

1 Introduction

In underground engineering, the stability of the tunnel surrounding rock is a critical factor affecting both engineering safety and economic efficiency (Zhu et al., 2016). Specifically, the unique stress conditions and complex surrounding rock structures of tunnel sidewalls significantly influence overall stability (Feng et al., 2018; Fraldi et al., 2019; Wu et al., 2024). As the depth of mineral resource extraction increases, elevated in-situ stress levels lead to more complex deformation and failure characteristics of the surrounding rock, making the sidewalls one of the most stress-concentrated and severely deformed regions (X. Zhang et al., 2024; Wang et al., 2025). The stability of an underground tunnel is often controlled by the mechanical properties and structure of the rock mass (Z. Zhao et al., 2023; Fan et al., 2023). In underground excavation, the tunnel sidewalls may pass through intact rock, simple jointed rock, or complex jointed rock, as shown in Fig. 1. When the excavation passes through intact or single-jointed rock, the tunnel stability is primarily influenced by the mechanical properties of the rock mass, with minimal impact from the rock structure (Zhu et al., 2020; M. Liu et al., 2024; Yang et al., 2024; F. Zhao et al., 2023). In contrast, complex

* Corresponding author.
E-mail address: dukuncsu@csu.edu.cn (K. Du).
Peer review under the responsibility of Tongji University

https://doi.org/10.1016/j.undsp.2025.05.008

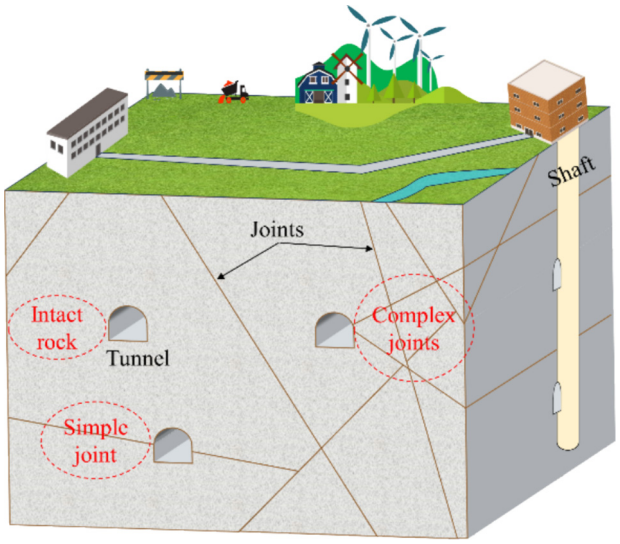

Fig. 1. Underground tunnel excavation and joint distribution.

interlocking joints divide the rock mass into wedge blocks of varying sizes and shapes (Bi et al., 2024; Fan et al., 2020). When these wedge blocks intersect with the tunnel sidewalls, the stability of the tunnel is significantly influenced by the wedge blocks (Wu et al., 2018).

For intact and simple jointed rock masses, researchers have studied the failure modes of tunnel sidewalls through laboratory experiments, numerical simulations, and theoretical analyses. The failure mode and characteristics of roadway sidewall were significantly influenced by the horizontal stress (Shi et al., 2024; Li et al., 2024; Ji et al., 2024). For wedge rock blocks formed by complex jointing, Hu et al. (2023) studied the instability mechanism of the wedge blocks and analyzed the evolution patterns of acoustic emission (AE) and intrinsic frequency information during the instability process. Yang et al. (2023) monitored the collapse process of wedge blocks and proposed a three-color early warning method for tunnel surrounding rock block collapse based on dynamic characteristic parameters. However, the study only focused on the instability modes and sliding mechanisms of wedge blocks, without investigating the mechanical response of the tunnel sidewall wedge blocks and the surrounding rock.

The distribution of surrounding rock structures, such as discontinuity characteristics, structural surfaces, and wedge blocks, further exacerbates the effects of stress concentration. This is especially true in deep engineering projects with high in-situ stresses, where the tunnel sidewall is more susceptible to tensile and shear failure (Jiang et al., 2022; Feng et al., 2017). Existing studies indicate that the presence of the stress concentration zone in the tunnel sidewalls causes the failure mode and instability mechanism to differ significantly from other parts of the tunnel (Li et al., 2017). Under the effect of stress concentration, the tunnel sidewall is prone to issues such as wedge block sliding and shear failure of structural surfaces, which may progressively evolve from localized damage to overall instability. Additionally, the joint orientation, in-situ stress, and their relationship with the tunnel axis significantly affect the failure of tunnel sidewalls (X. Liu et al., 2024; B. Liu et al., 2024). Therefore, a comprehensive study of the stress evolution characteristics in the tunnel sidewall and its impact on surrounding rock stability is of significant theoretical and practical importance for ensuring tunnel safety.

Based on the above background, the physical model of tunnel sidewalls containing wedge blocks under biaxial stress conditions was modeled. The influence of cracks and fractures on the stability of rock masses was investigated. The mechanical mechanisms of interaction between different wedge blocks and the surrounding rock and their impact on the stability of tunnel sidewalls were investigated. In addition, discrete element numerical simulation techniques were employed to further explore the dynamic evolution characteristics of tensile and shear stresses at the boundaries of wedge blocks and arched holes. Furthermore, this paper discusses the failure modes of wedge blocks and arched holes under different horizontal in-situ stress conditions, clarifying the stress sensitivity of failure characteristics, and providing important references for the stability design of tunnel sidewalls in deep engineering projects.

2 Wedge blocks analysis

In the mechanical analysis, the wedge block was treated as a continuum medium, and its material behavior was characterized using an elastic–plastic constitutive model. The sliding or detachment of the wedge block was predominantly governed by the joint surface strength. The joint surface was subjected to compressive stress in the normal direction, while its tangential behavior followed the Mohr–Coulomb criterion. The position and orientation of the joints control the shape and type of these wedge blocks. Without the loss of generality, the geometry of a rock block right a tunnel is shown in Fig. 2. Multiple joint surfaces and the tunnel side form a finite block. Joints 1 and 2 intersect with the tunnel side at points A and B, with

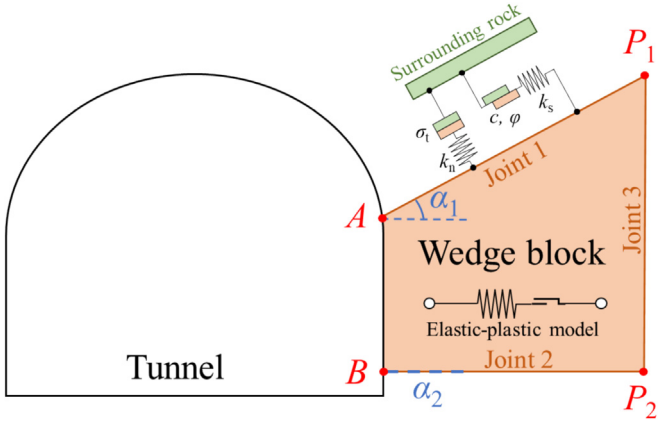

Fig. 2. Wedge block and tunnel cross-section.

corresponding inclination angles of α_1 and α_2. Joint 3 intersects with joints 1 and 2 inside the rock mass, and the corresponding intersection points are P_1 and P_2.

It is assumed that the counterclockwise angle between the joint surface and the horizontal plane is positive, while the clockwise angle is negative. The wedge blocks are classified into triangular and quadrilateral types based on the shape of their cross-section. Table 1 presents several typical methods of analyzing wedge block types. When points P_1 and P_2 coincide, it is like specimen "S1". When the length of P_1P_2 is less than or equal to the length of AB, it is like specimen "S2". When points A and B coincide, it is like specimen "S3". When the length of P_1P_2 exceeds the length of AB, it is like specimen "S4". At the junction between the wedge block in the tunnel sidewall and the free face, a horizontal column is formed within the rock mass. The intersection points of the joint surface and the tunnel are labeled A, B, C, and D, while the apexes of the block within the rock mass are labeled P_1, P_2, P_3, and P_4. In the horizontal direction within the podetium, the projection of $ABCD$ is denoted as $A'B'C'D'$, and the projection of $P_1P_2P_3P_4$ is denoted as $P'_1P'_2P'_3P'_4$. If $S_{P'_1P'_2P'_3P'_4} < S_{A'B'C'D'}$, and $P'_2P'_3$ is located below $B'C'$, then the wedge block is a stable block, as in specimen "S2". If $P'_1(P'_2)P'_3(P'_4)$ is located below $B'C'$ and no plane can be formed, the wedge block is also a stable block, as in specimen "S1". If $S_{P'_1P'_2P'_3P'_4} > S_{A'B'C'D'}$, the wedge block is an extremely stable

Table 1
Typical wedge block type analysis.

Specimen No.	Typical wedge blocks	Wedge blocks and apex spatial position	Characteristics	Type
S1	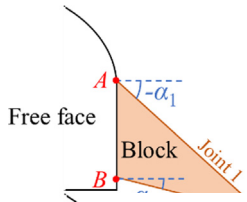	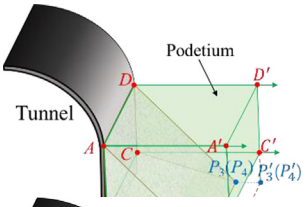	α_1, $\alpha_2 \neq 0$, $\alpha_1 > \alpha_2$, $P'_1(P'_2)P'_3(P'_4) \notin A'B'C'D'$, $P'_1(P'_2)P'_3(P'_4)$ is below $B'C'$.	Stable triangular block
S2	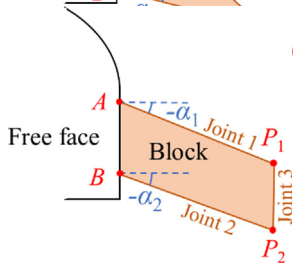	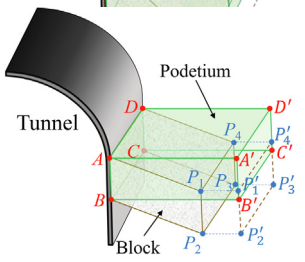	α_1, $\alpha_2 \neq 0$, $\alpha_1 > \alpha_2$, $S_{P'_1P'_2P'_3P'_4} < S_{A'B'C'D'}$, $P'_2P'_3$ is below $B'C'$.	Stable quadrilateral block
S3	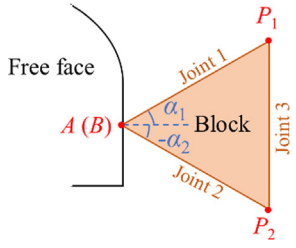	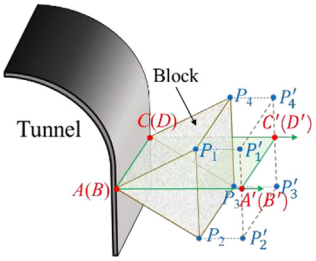	α_1, $\alpha_2 > 0$, $P'_1P'_2P'_3P'_4 \ni A'(B')C'(D')$	Extremely stable triangular block
S4	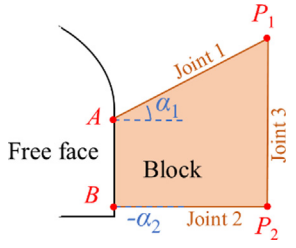	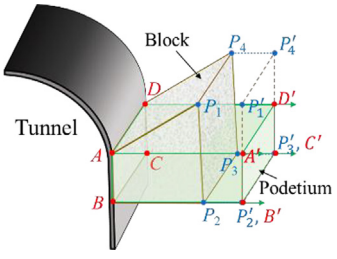	α_1, $\alpha_2 \geq 0$, $S_{P'_1P'_2P'_3P'_4} > S_{A'B'C'D'}$	Extremely stable quadrilateral block

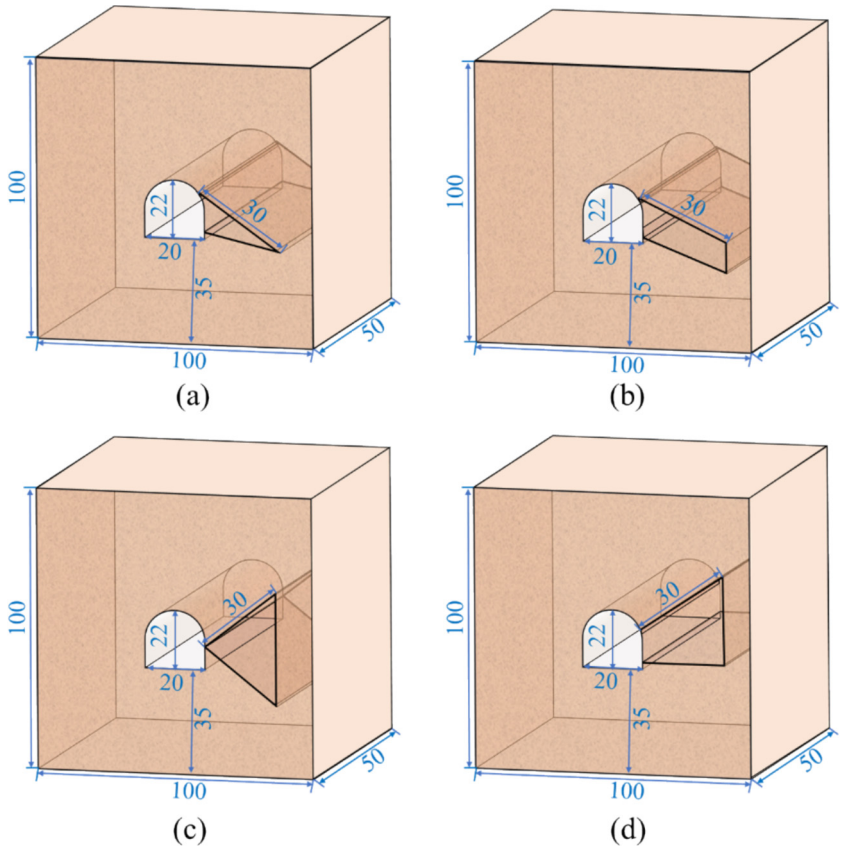

Fig. 3. Specimen and wedge block size scheme. (a) S1, (b) S2, (c) S3, and (d) S4. (Unit: mm)

block, as in specimen "S4". Similarly, if the intersection of the tunnel sidewall cannot form a prism, the wedge block is also classified as an extremely stable block, as in specimen "S3".

3 Experimental methodologies and results

3.1 Experimental methodologies

3.1.1 Specimens design

Different types and shapes of wedge blocks were designed at the sidewall of the hole, as shown in Fig. 3. On the right sidewall of the hole, a stable triangular block with a maximum side length of 30 mm was pre-fabricated. The stable triangular block, extremely stable triangular block, stable quadrilateral block, and extremely stable quadrilateral block correspond to specimens "S1", "S2", "S3", and "S4", respectively.

3.1.2 Specimens making

The experimental material used was rock-like material, consisting of C42.5 ordinary portland cement, fine river sand, and water in a weight ratio of 2:2:1. Before pouring, an arched iron block with dimensions of 100 mm in length, 20 mm in width, and 22 mm in height was placed at the center of the mold. After thoroughly mixing the materials, the mixture was poured into a 100 mm × 100 mm × 100 mm cubic mold, with the pouring height set to half the height of the mold. On the right sidewall of the arched hole, a joint fissure was created using insert-and-pull steel plates. The steel plates had dimensions of 100 mm in length, 30 mm in width, and 0.5 mm in thickness. After pouring, the arched iron block and steel plates were removed 2 h later. After one day of solidification, the specimen was demoulded and placed in a constant temperature and humidity curing box for 28 days. After curing, the surface of the specimen and the arched hole were repeatedly polished until smooth. After processing, the measured specimen dimension deviation did not exceed 1 mm. The specimen fabrication process is shown in Fig. 4(a). The attached layer of the digital image method was marked before the experiment, as shown in Fig. 4(b). Firstly, white spray paint was used to spray a uniform primer on the specimen surface as a background layer. Secondly, black spray paint was used to spray the speckle layer, and high contrast speckles were formed by spraying random dots.

3.1.3 Experimental system and loading conditions

The experimental system used in this study consists of a biaxial mechanical testing system, an AE system, and a digital image correlation (DIC) system, as shown in Fig. 5. The mechanical system utilizes a universal testing machine (INSTRON 1346) with a maximum vertical load of 2000

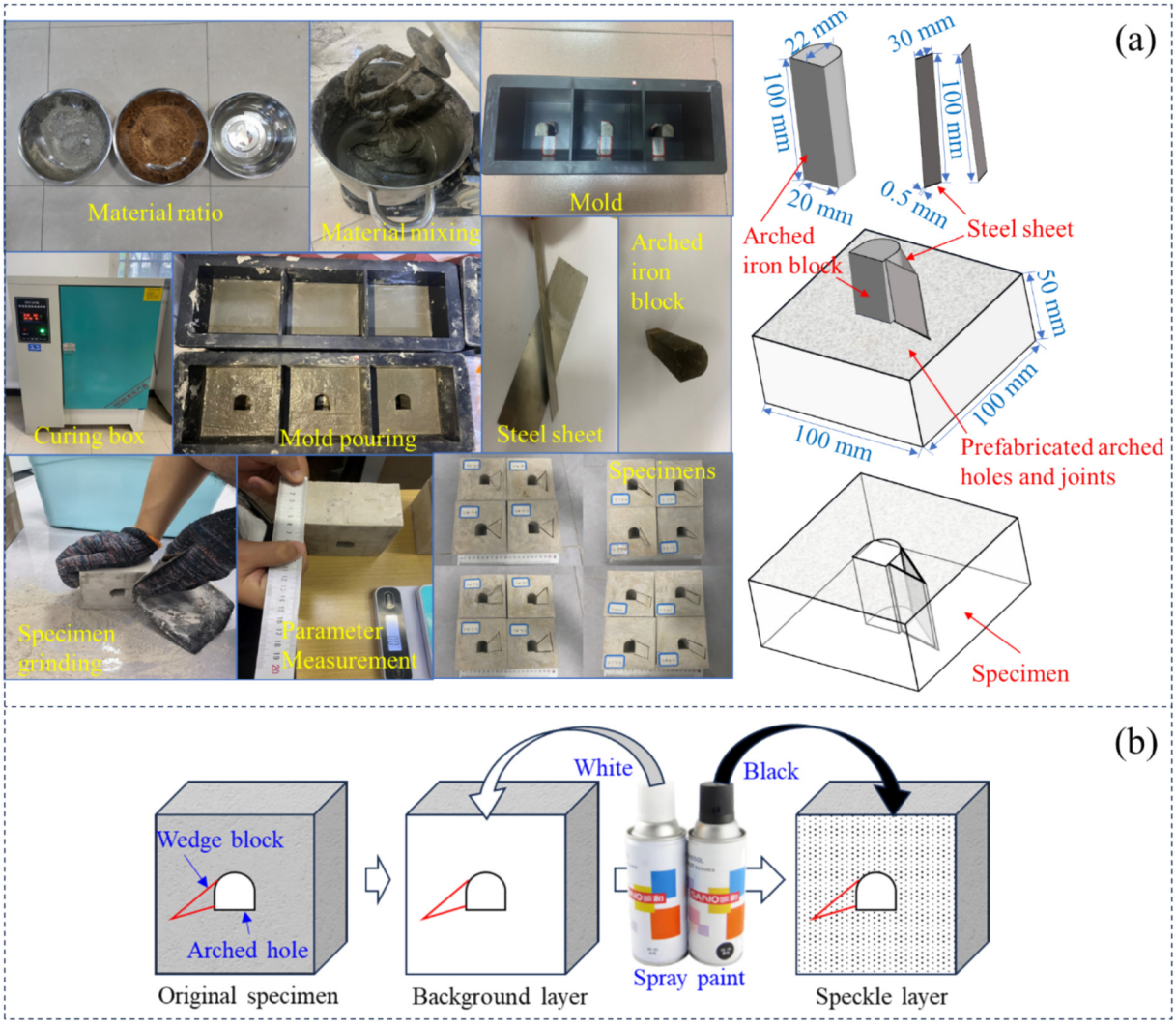

Fig. 4. Specimen fabrication and speckle marking process. (a) Specimen fabrication process, and (b) speckle marking process.

kN, a horizontal load of 250 kN, a load accuracy of ±0.5%, and a piston stroke of ±50 mm. The control modes include displacement, load, and strain. The AE system employs the PCI-2 model, which includes amplifiers, sensors, and a computer, as shown in Fig. 5(a). The main amplifier is set to 40 dB, with a threshold of 45 dB. The waveform sampling length is 32 000, and the sampling rate is 5 MSPS (millions of samples per second). To ensure the accuracy of the test results, four AE sensors are used for each specimen. The DIC system includes a camera, high-intensity light, and a computer, with a maximum recording speed of 60 frames per second, as shown in Fig. 5(b). The experiment was conducted using biaxial compression, with loading applied simultaneously in the z and y directions to 3 MPa. The y-direction stress was maintained constant, while the z-direction stress continued to increase until specimen failure, as shown in Fig. 5(c). The stress in the z-direction was denoted as σ_1, and the stress in the y-direction was denoted as σ_3. A displacement-controlled loading method was used, with a loading rate of 0.15 mm/min. The DIC image acquisition was set to capture 10 frames per second. All data collection started and ended simultaneously. During the experiment, different specimens were tested under both unsupported and supported conditions. The experimental loading conditions are shown in Fig. 5(d). Unsupported is the specimen's arched hole as a free surface. The supported is to simulate the passive support of the steel arch of the roadway by placing an iron block of equal volume inside the arched hole.

3.2 Experimental results

3.2.1 Mechanical parameters

The results of the biaxial compression tests are shown in Table 2. σ_{bcs} represents the maximum failure strength of the biaxial compression specimen, and E_1 is the elastic modulus during the σ_1 loading process. The average σ_{bcs} and average E_1 values for both unsupported and supported specimens are shown in Fig. 6. Under unsupported conditions, the average σ_{bcs} and average E_1 of the extremely stable specimens ("S3" and "S4") were greater than those

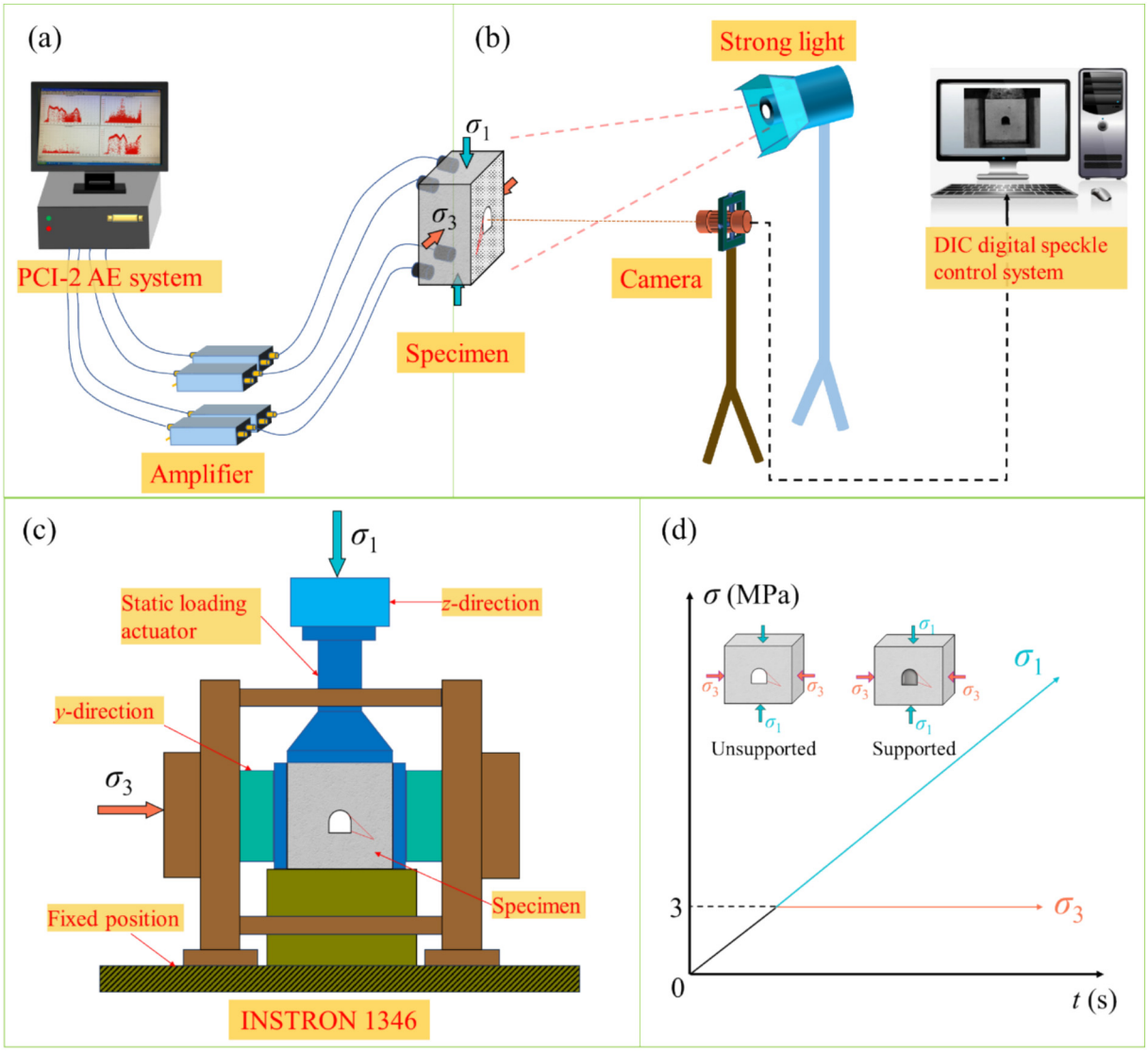

Fig. 5. Experimental test system. (a) PCI-2 AE system, (b) DIC system, (c) biaxial test system, and (d) biaxial stress loading path.

Table 2
Results of biaxial compression tests.

No.	Block type	Block shape	Supported (Y/N)	Density (kg/m^3)	E_1 (GPa)	σ_{bcs} (MPa)
S1-1	Stable	Triangular	N	2018.41	2.93	26.76
S1-2	Stable	Triangular	N	1967.65	3.28	27.47
S1S-1	Stable	Triangular	Y	1928.49	3.52	33.79
S1S-2	Stable	Triangular	Y	1950.79	4.08	43.06
S2-1	Stable	Quadrangular	N	1879.00	3.11	25.31
S2-2	Stable	Quadrangular	N	2001.67	3.23	27.37
S2S-1	Stable	Quadrangular	Y	2030.89	3.62	36.90
S2S-2	Stable	Quadrangular	Y	1990.12	3.28	35.81
S3-1	Extremely stable	Triangular	N	2079.26	4.55	37.44
S3-2	Extremely stable	Triangular	N	2058.79	4.16	32.84
S3S-1	Extremely stable	Triangular	Y	2139.41	4.19	41.38
S3S-2	Extremely stable	Triangular	Y	2041.43	3.26	32.89
S4-1	Extremely stable	Quadrangular	N	2028.94	3.98	30.76
S4-2	Extremely stable	Quadrangular	N	1982.35	3.42	26.87
S4S-1	Extremely stable	Quadrangular	Y	1930.59	3.87	34.68
S4S-2	Extremely stable	Quadrangular	Y	2002.47	3.88	35.35

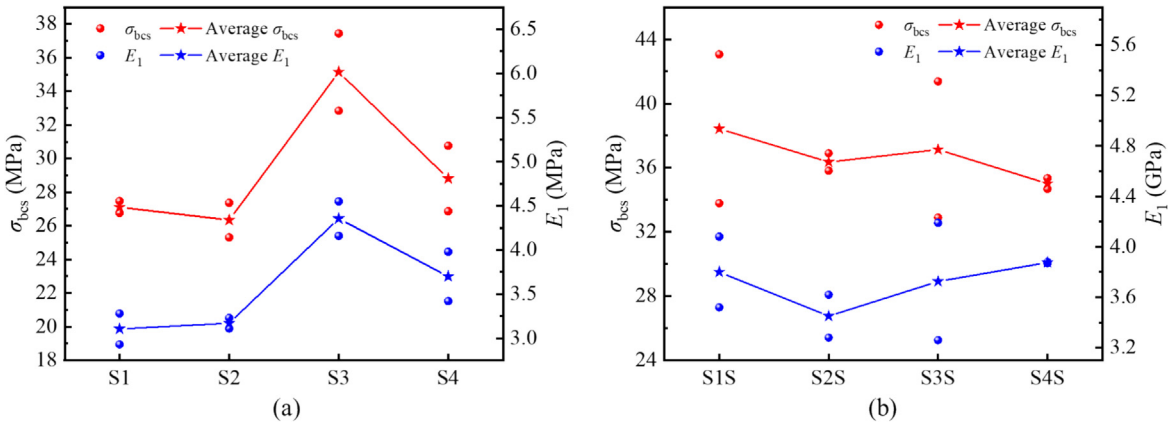

Fig. 6. Average σ_{bcs} and average E_1 of different specimens. (a) Unsupported specimen, and (b) supported specimen.

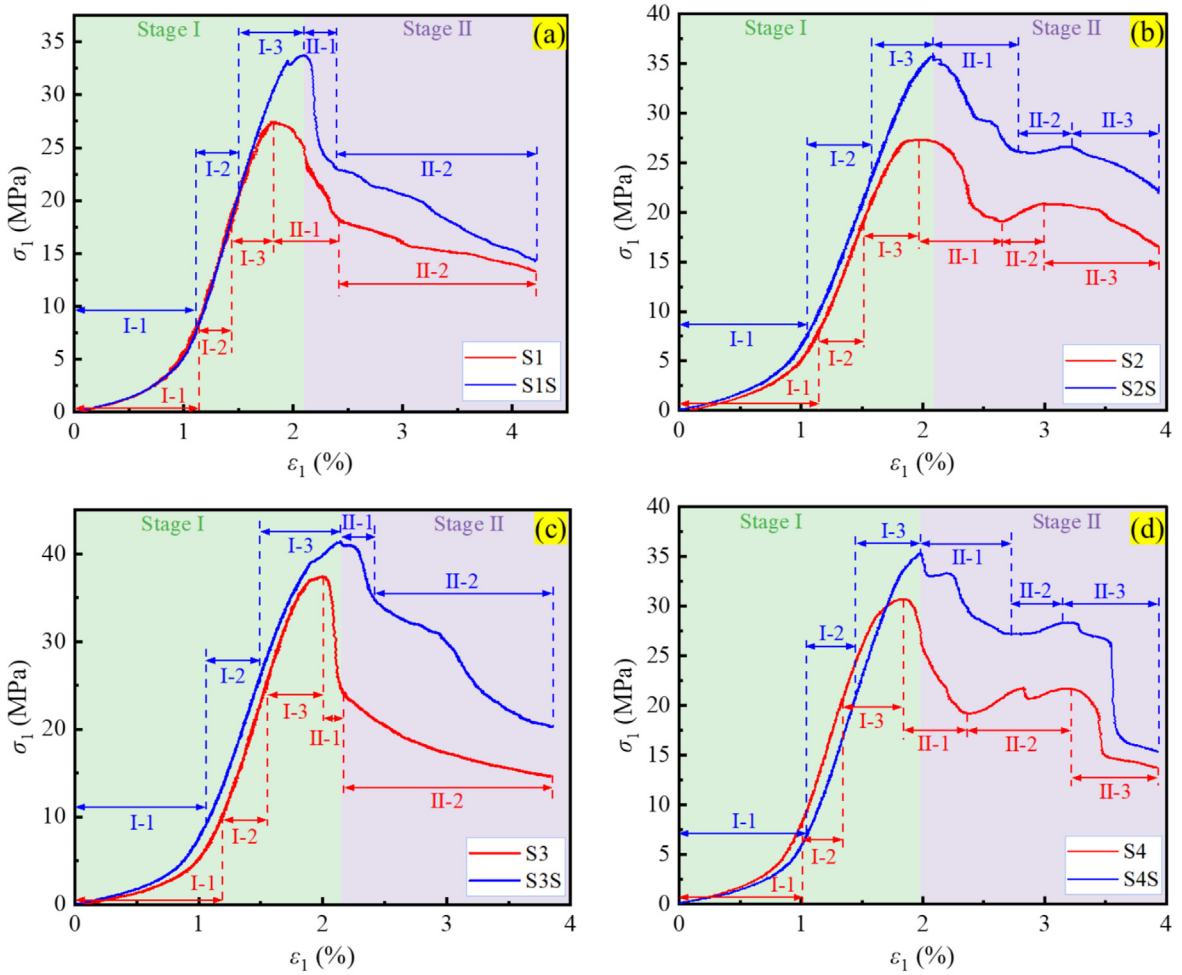

Fig. 7. Stress–strain curves of different specimens. (a) Stable triangular block, (b) stable quadrilateral block, (c) extremely stable triangular block, and (d) extremely stable quadrilateral block.

of the stable specimens ("S1" and "S2"), as shown in Fig. 6 (a). After support, the average σ_{bcs} of specimen "S1S" and the average E_1 of specimen "S4S" were the highest, while the average σ_{bcs} of specimen "S4S" and the average E_1 of specimen "S2S" were the lowest, as shown in Fig. 6(b).

3.2.2 Stress–strain curves

In the biaxial compression test, the rock-like material primarily underwent two stages: Stage I represented the stress–strain curve before reaching the peak stress, while Stage II represented the curve after the peak stress, as

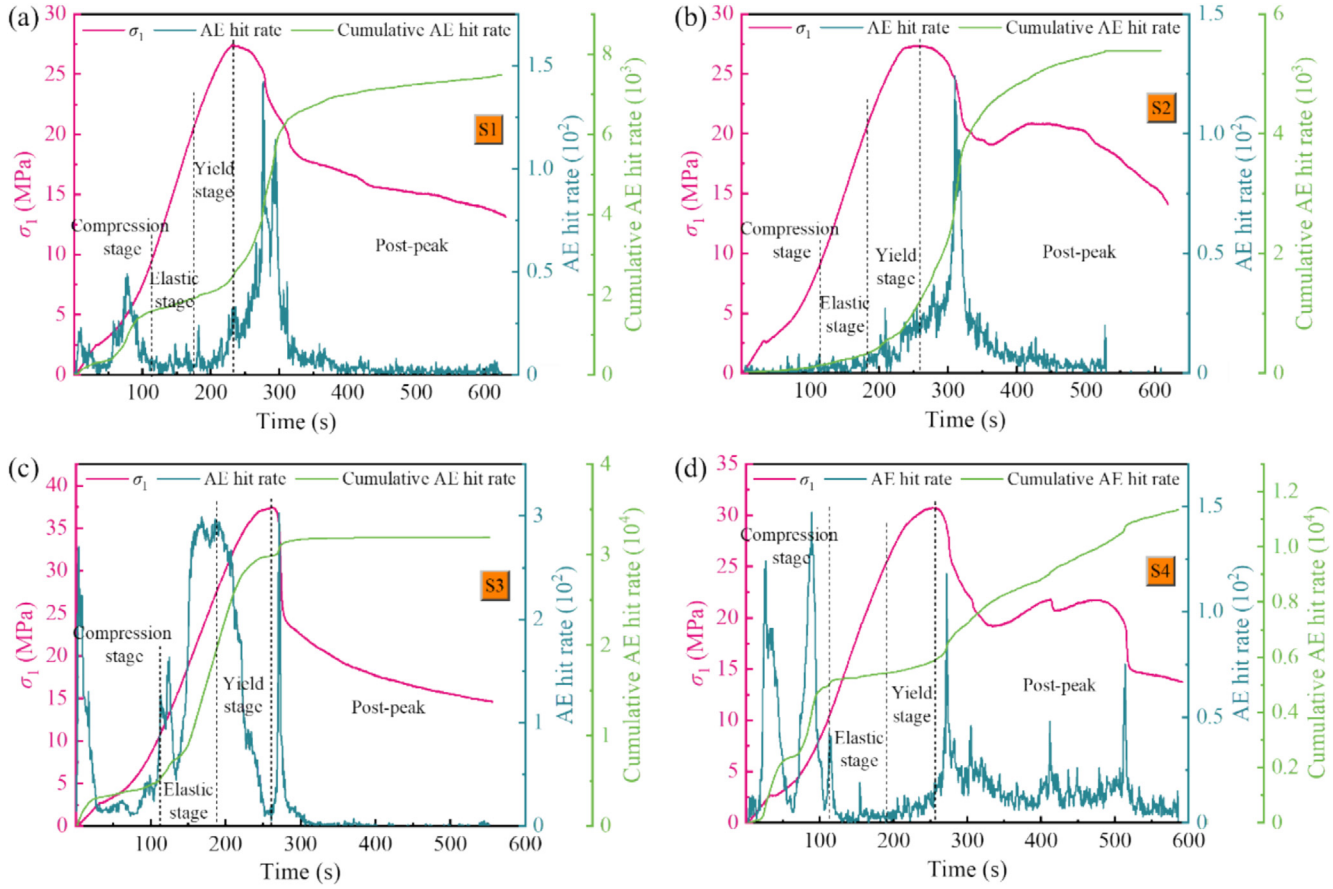

Fig. 8. AE hit rate of unsupported specimens. (a) S1, (b) S2, (c) S3, and (d) S4.

shown in Fig. 7. In Stage I, all the specimens experienced three phases: I-1 (compression phase), I-2 (elastic phase), and I-3 (yield phase). During phase I-1, the pre-existing microcracks inside the specimens closed under the initial stress, and the curve exhibited a concave-up shape, accelerating upwards. In phase I-2, the material underwent elastic deformation, and the curve increased almost linearly. The phase I-3 corresponded to the development and propagation of new cracks, with the curve showing a convex-up shape and a reduced rate of increase. The endpoint of this phase represented the peak value of the specimen's failure. Different types of specimens exhibited distinct mechanical properties during Stage II. In Fig. 7(a), the peak value of specimen "S1S" was higher than that of "S1". During phase II-1, microcrack penetration occurred, and the peak value rapidly decreased. In contrast, during phase II-2, crack surface sliding took place, where the rate of strength reduction decreased and the strain value increased. In Fig. 7(b), the peak value of specimen "S2S" was higher than that of "S2". During phase II-1, microcrack penetration occurred, and the peak rapidly decreased. In phase II-2, interlocking between the wedge and the surrounding rock created an increased strength. Subsequently, in phase II-3, crack surface sliding occurred, and the curve gradually decreased. In Fig. 7(c), the peak value of specimen "S3S" was higher than that of "S3". During phase II-1, microcrack penetration occurred, and the peak value rapidly decreased. In contrast, during phase II-2, crack surface sliding took place, leading to a reduction in the rate of strength decline and an increase in strain. In Fig. 7(d), the peak value of specimen "S4S" was higher than that of "S4". During phase II-1, microcrack penetration occurred, and the peak value rapidly decreased. In phase II-2, interlocking between the wedge and the surrounding rock created an increased strength. Subsequently, during phase II-3, crack surface sliding and macrocrack extension occurred, with the curve initially declining slowly, followed by a rapid decline, and finally slowing down again. It can be concluded that the peak values and post-peak behaviors of the supported specimens were higher than those of the unsupported specimens. In addition, after the peak, the effect on the mechanical behavior of the stable wedge blocks was not significant, while the extremely stable wedge blocks produced a significant effect.

3.2.3 AE hit rate

The AE hit rate, as an important characteristic parameter, can reflect the intensity of AE activity and the internal cracking of the rock-like specimens. The variation of the AE hit rate with time during the biaxial compression of

the unsupported specimens is shown in Fig. 8. Previous studies have shown that during the compression, elasticity, yield and post-peak phases, the acoustic emission occurred sequentially in the AE active, quiet, rising and globally active phases (Zhang & Zhou, 2020; Du et al., 2020a). However, different stages of AE hits pre-peak stress exhibited different characteristics due to the effect of different wedge block types. During the compression phase, wedge blocks in specimens "S1", "S3", and "S4" experienced sliding against the surrounding rock, resulting in early-stage peaks in AE hit rate curves (locally active period). In contrast, the wedge block in specimen "S2" maintained stability with the surrounding rock. During the elastic stage, specimens "S1", "S2", and "S4" exhibited stable periods in their AE hit rates, while specimen "S3" showed two distinct peaks in its AE hit rate curve due to sliding between the wedge block and surrounding rock. During the yielding stage, specimens "S1", "S2", and "S4" exhibited continuous growth of new fractures, with their AE hit rate curves showing a stable growth phase. In contrast, specimen "S3" demonstrated reduced crack propagation rates, resulting in a descending AE hit rate curve that reached a distinct trough (suppression phase). After the peak, the cracks in the specimen were penetrated, and the whole was destabilized, and the AE hit rate showed a globally active period. It can be seen that the AE hit rate characteristics after the stress peak were mainly caused by the overall instability of the specimen, while the AE hit rate characteristics at different stages before the peak were caused by different types of wedge blocks.

The variation of the AE hit rate with time during the biaxial compression of the supported specimen is shown in Fig. 9. During the compression phase, the specimens "S1S", "S3S", and "S4S" showed locally stable periods, while the wedge of specimen "S2S" had a locally active period of sliding against the surrounding rock. During the elastic stage, the AE hit rate maintained a locally stable period. During the yield stage, the new cracks grew, and the AE hit rate curves increased to different degrees, with the fastest increase in specimen "S4S". After the peak, the cracks in the specimen were penetrated, and the whole was destabilized, and the AE hit rate showed a globally active period. It can be seen that the wedge blocks did not affect the pre-peak stress stage in most of the specimens after the support. Only the compression phase of specimen "S2S" produced locally active acoustic emission impact rates, which was the opposite of the unsupported condition.

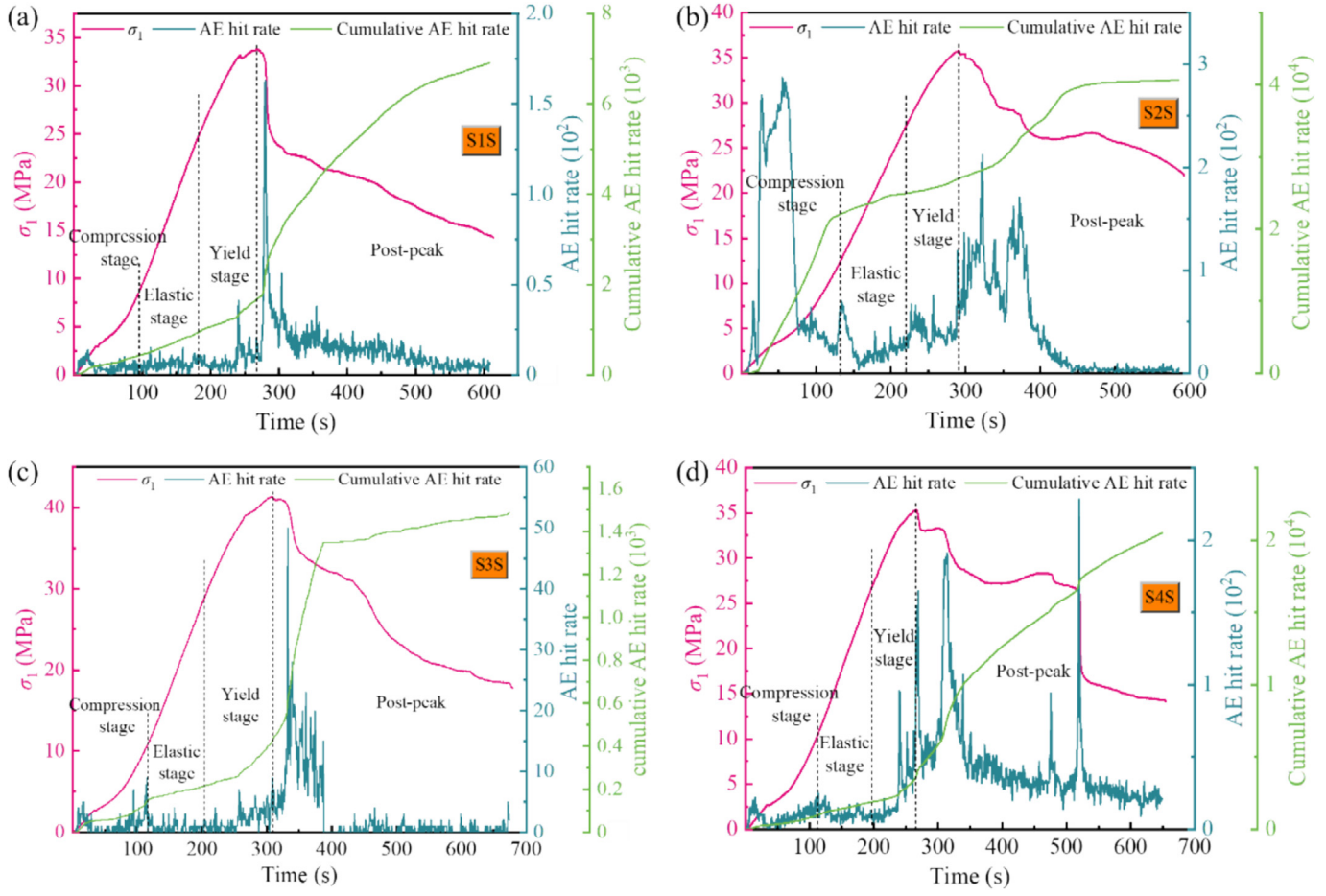

Fig. 9. AE hit rate of supported specimens. (a) S1S, (b) S2S, (c) S3S, and (d) S4S.

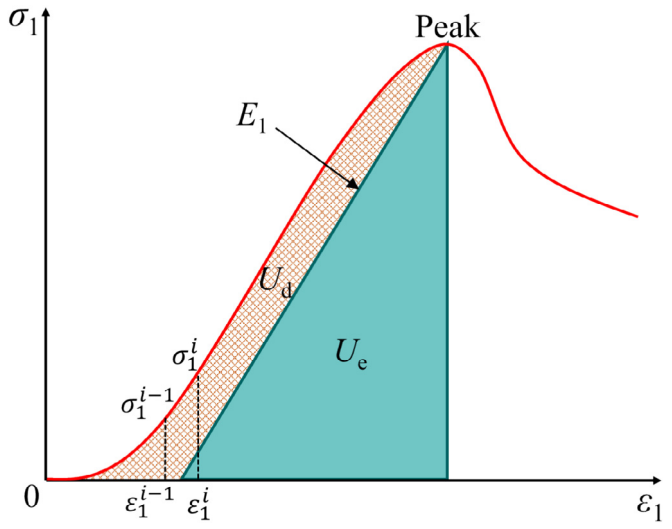

Fig. 10. Relationship between elastic strain energy and dissipated energy.

3.2.4 Energy evolution mechanism

Assume that the tested rock-like specimens and the biaxial mechanical testing machine form a closed system that does not exchange energy with the external environment (W. Zhang et al., 2024). The relationship between the total strain energy (U), elastic strain energy (U_e), and dissipated energy (U_d) during the loading process of the rock-like specimen is shown in Fig. 10.

The total strain energy is calculated as in Eq. (1):

$$U = U_e + U_d. \tag{1}$$

The energy in the spatial stress state is Eq. (2):

$$U = \sum_{i=1}^{n} \frac{1}{2}\left(\sigma_1^i + \sigma_1^{i-1}\right)\left(\varepsilon_1^i - \varepsilon_1^{i-1}\right). \tag{2}$$

After simplification, the formulas for calculating the energy of each component within the rock-like material are Eqs. (3) and (4):

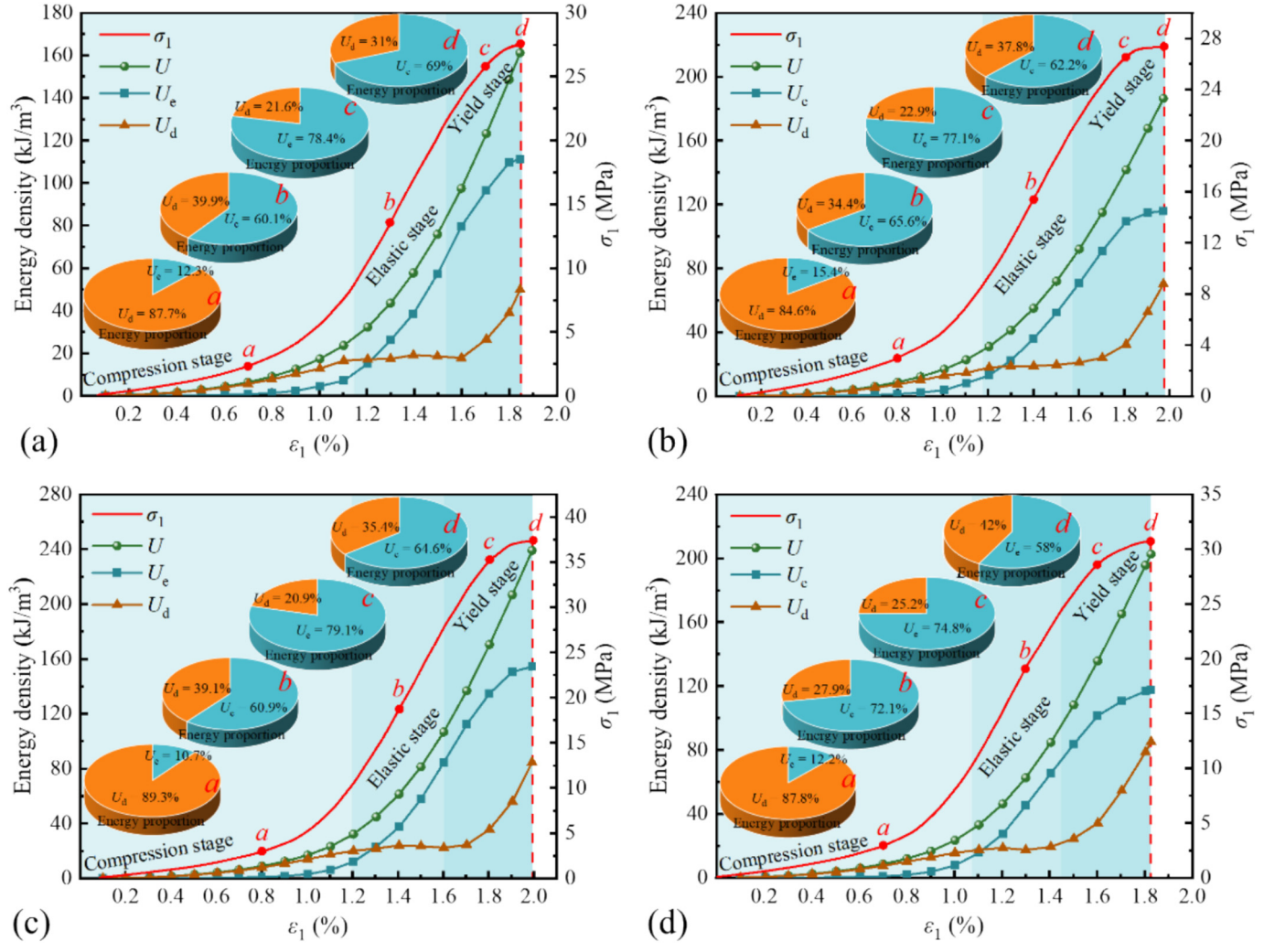

Fig. 11. Energy characteristics of unsupported specimens. (a) S1, (b) S2, (c) S3, and (d) S4.

$$U_e = \frac{\sigma_1^2}{2E_1}, \tag{3}$$

$$U_d = U - U_e. \tag{4}$$

The energy evolution curve and the energy percentage at different stages are shown in Figs. 11 and 12. During the compression phase, as σ_1 increased, U, U_e, and U_d gradually increased. In the elastic phase, the slope of the U_d curve decreased and approached a horizontal line, while the curves for U and U_e were similar, with their slopes gradually increasing. In the yielding phase, the rate of increase of U_d accelerated, and its curve became concave upwards. The U increased at a constant rate, with its curve being a straight line, while the growth rate of U_e gradually decreased, and its curve became convex upwards. Additionally, points *a*, *b*, *c*, and *d* were selected at the compression phase, elastic phase, yielding phase, and peak value, respectively, and the energy percentages for each phase were calculated. During the compression phase, the percentage of U_d was greater than that of U_e, primarily due to the closure of internal microcracks during this phase. In the elastic phase, the percentage of U_e was greater than the U_d, indicating that the U input by the testing machine was mainly stored in the specimen as U_e. In the yielding phase, the percentage of U_e continued to increase, but the rate of increase slowed. This was mainly because most of the input energy was stored as U_e and had nearly reached the storage limit. At the peak value, the percentage of U_e decreased. This was primarily because the input energy exceeded the specimen's bearing limit, causing the accumulated U_e to be rapidly released as U_d, leading to the rapid expansion of microcracks into macrocracks. After support, the U at the peak of specimens increased. This was because the bearing capacity of the specimens increased, leading to a corresponding increase in the stored U_e.

3.2.5 Strain field evolution

DIC technology identifies surface strain field characteristics by observing changes in the velocity and displacement of microscopic particles. By analyzing the relative motion of velocity vector trend lines, it is possible to distinguish between lateral strain (E_{xx}) and shear strain (E_{xy}) concentration zones. Measurement points are set on both sides of the strain concentration zone, and the velocity vector

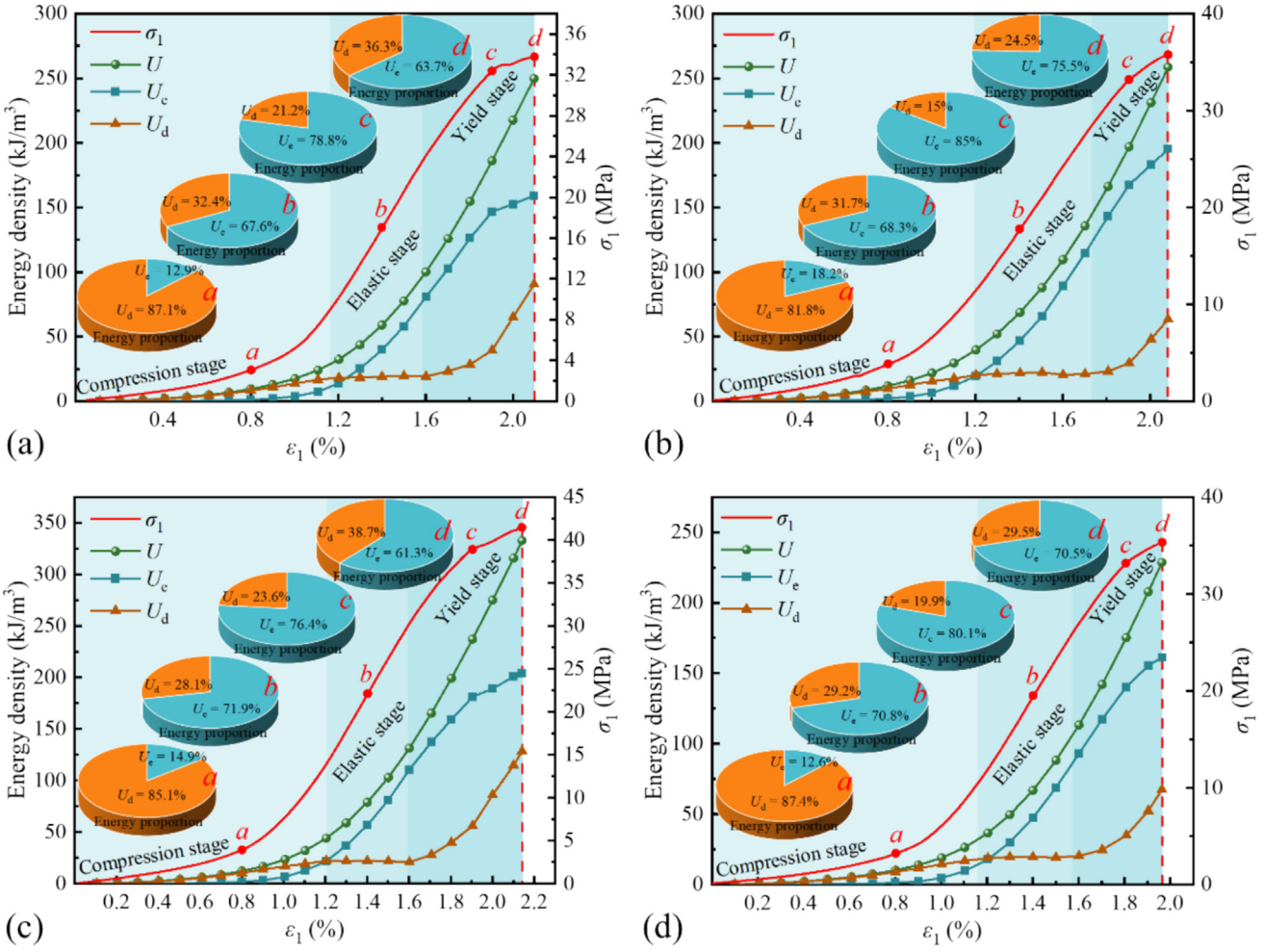

Fig. 12. Energy characteristics of supported specimens. (a) S1S, (b) S2S, (c) S3S, and (d) S4S.

is decomposed into the x-component in the vertical direction and the y-component in the parallel direction, allowing for a direct comparison of their directions and magnitudes (Zhang et al., 2023; Liu et al., 2022), as shown in Fig. 13.

The strain values at the midpoints of each stage before the peak in the stress–strain curves of the specimens were analyzed. For the unsupported specimens, the E_{xy} and E_{xx} corresponding to the compression, elastic, yield stages, and peak value are shown in Table 3. In the compression stage, the E_{xy} and E_{xx} of the specimens did not exhibit obvious strain concentration zones. In the elastic stage, specimen "S1" displayed larger strain values near the block boundaries, while no significant strain concentration was observed in the other specimens. During the yield stage, specimens "S1" and "S4" exhibited larger strain values near the block boundaries, while specimen "S2" showed significant strain near the wedge block and around the arched hole, extending to the lower right corner of the specimen. Specimen "S3" demonstrated larger strain values at the top and bottom of the arched hole, as well as at the top and bottom corners on the right side of the specimen. At the peak, the strain values for all specimens continued to increase, with the strain zones becoming interconnected and their range expanding.

For the supported specimens, the E_{xy} and E_{xx} corresponding to the compression, elastic, yield stages, and peak values are shown in Table 4. During the compression phase, no significant strain concentration zones were observed for E_{xy} and E_{xx}. In the elastic phase, specimen "S4S" exhibited relatively high strain values near the wedge block and around the arched hole, while other specimens showed large strain values around the arched hole. During the yielding phase, specimens "S1S" and "S4S" showed relatively high strain values near the wedge block, specimen "S2S" exhibited large strain values around the arched hole, and specimen "S3S" had larger strains on the right side of the arched hole, extending to the right boundary of the specimen. At the peak, specimens "S2S" and "S4S" exhibited increased strain values near the wedge block and on the right side of the arched hole. The strain concentration zone near the wedge block in specimen "S1S" expanded, while the strain values in specimen "S3S" increased throughout the specimen.

4 Numerical simulation analysis

Universal Distinct Element Code (UDEC) is a widely used software for simulating the behavior of rocks and other discrete media. It utilizes the distinct element method (DEM) to model rock behavior that involves fractures, joints, and failure surfaces. The core of UDEC simulates rock mass failure through the contact mechanics between joints and blocks. During the model computation process, the software tracks the motion of each block, including both translation and rotation, and calculates the normal and shear forces acting on the joint surfaces. If the stress on a joint surface exceeds its strength, sliding, opening, or shear failure may occur, thereby simulating the rock mass failure process.

4.1 Model establishment and calibration

Two rectangular models, 100 mm × 50 mm and 100 mm × 100 mm, were established for uniaxial compression and biaxial compression tests. The initial material properties, including rock density, Young's modulus, Poisson's ratio, and other mechanical parameters, were input based on the available mechanical parameters of the rock specimens. Voronoi-Trigon blocks and a grid model were created, with block and grid sizes both set to 2 mm. The bottom of the model was fixed, vertical stress σ_1 was applied at the top, and horizontal stress σ_3 was applied at both sides. The stress paths were consistent with the experiments, and σ_1 and σ_3 were loaded simultaneously at a loading rate of 0.05 m/s up to 3 MPa, at which time σ_3 was kept constant, and σ_1 was continually loaded up to the destruction of the specimen. The parameters were calibrated repeatedly to obtain simulation curves that closely matched the experimental results, with peak stress and Young's modulus errors within 10%, as shown in Fig. 14. Different block types were generated in the arched hole by cutting multiple intersecting joint fractures. Rigid materials were used to simulate the support in this study. The simulation parameters include bulk modulus (K), shear modulus (G), normal stiffness (k_n), tangential stiffness (k_s), cohesion (c), friction angle (φ), and tensile strength (σ_t), as shown in Table 5.

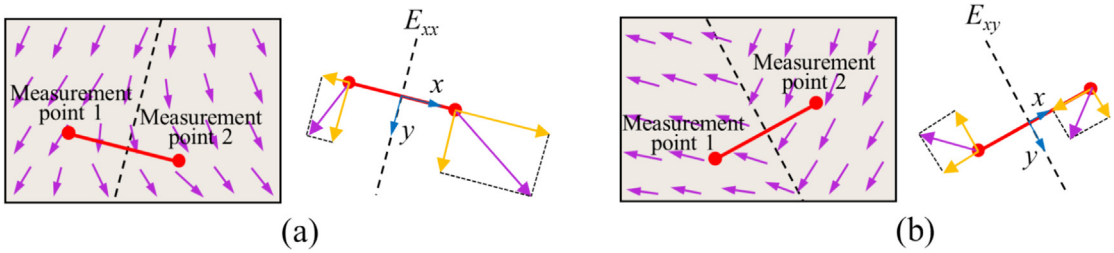

Fig. 13. Velocity vector field. (a) E_{xx}, and (b) E_{xy}.

Table 3
E_{xy} and E_{xx} of unsupported specimens at different stages.

Specimen No.	Strain type	Compression stage	Elastic stage	Yield stage	Peak
S1	E_{xy}	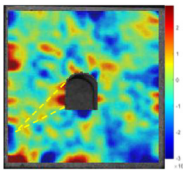	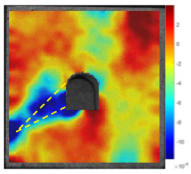	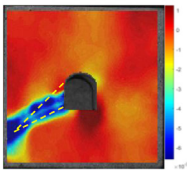	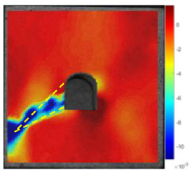
	E_{xx}	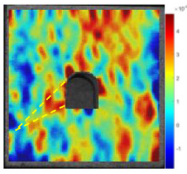	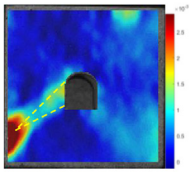	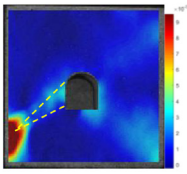	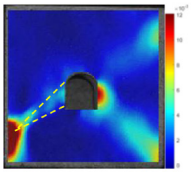
S2	E_{xy}	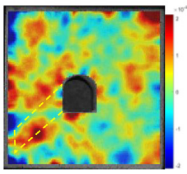	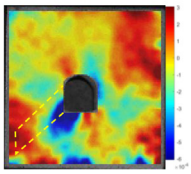	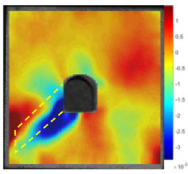	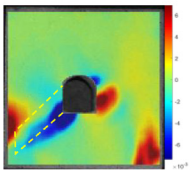
	E_{xx}	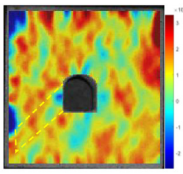	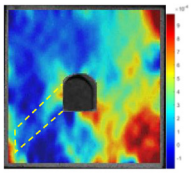	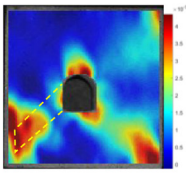	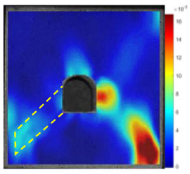
S3	E_{xy}	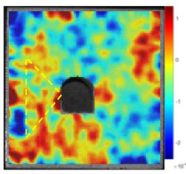	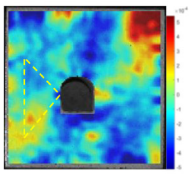	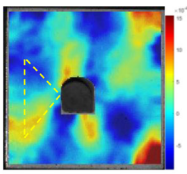	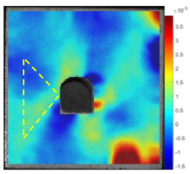
	E_{xx}	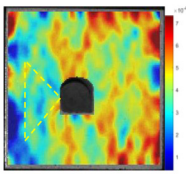	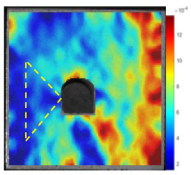	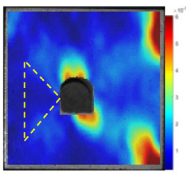	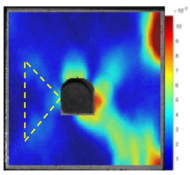
S4	E_{xy}	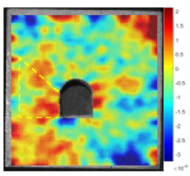	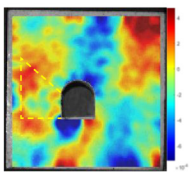	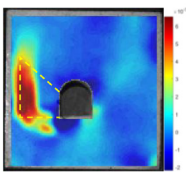	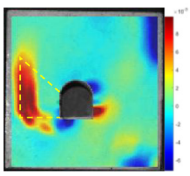
	E_{xx}	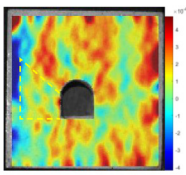	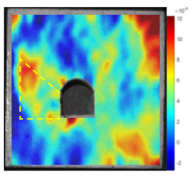	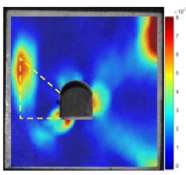	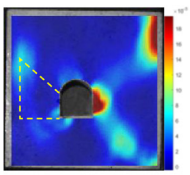

Table 4
E_{xy} and E_{xx} of supported specimens at different stages.

Specimen No.	Strain type	Compression stage	Elastic stage	Yield stage	Peak
S1S	E_{xy}	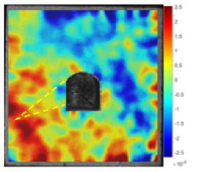	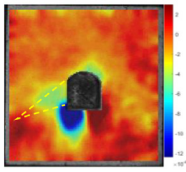	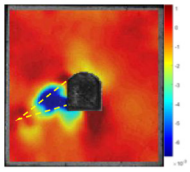	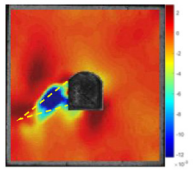
	E_{xx}	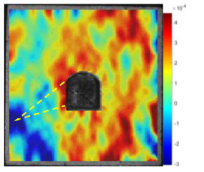	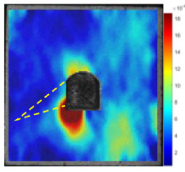	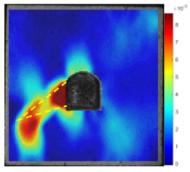	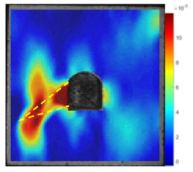
S2S	E_{xy}	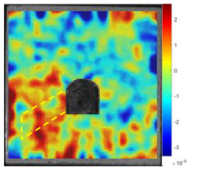	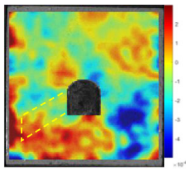	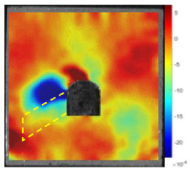	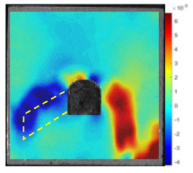
	E_{xx}	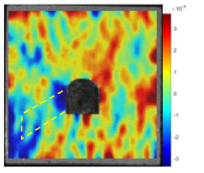	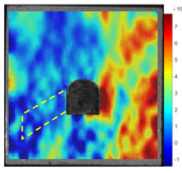	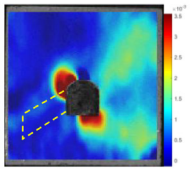	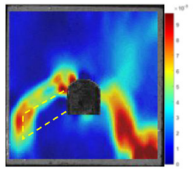
S3S	E_{xy}	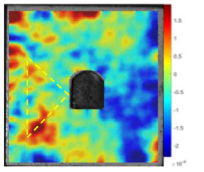	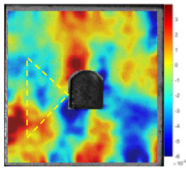	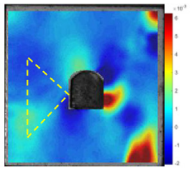	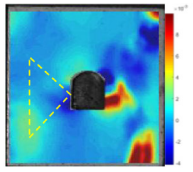
	E_{xx}	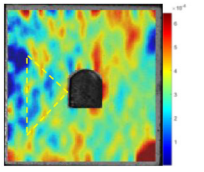	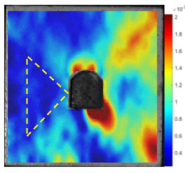	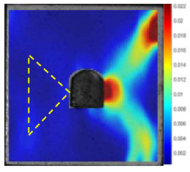	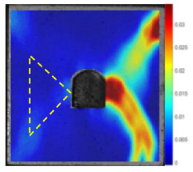
S4S	E_{xy}	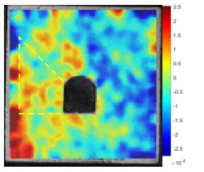	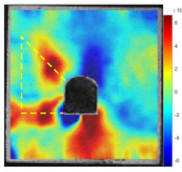	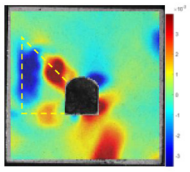	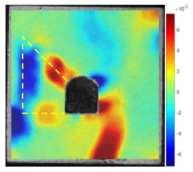
	E_{xx}	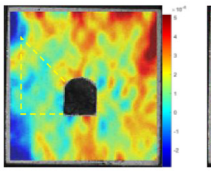	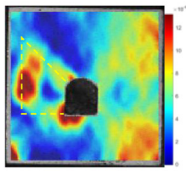	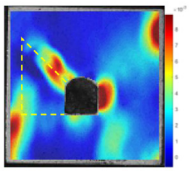	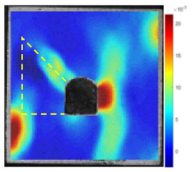

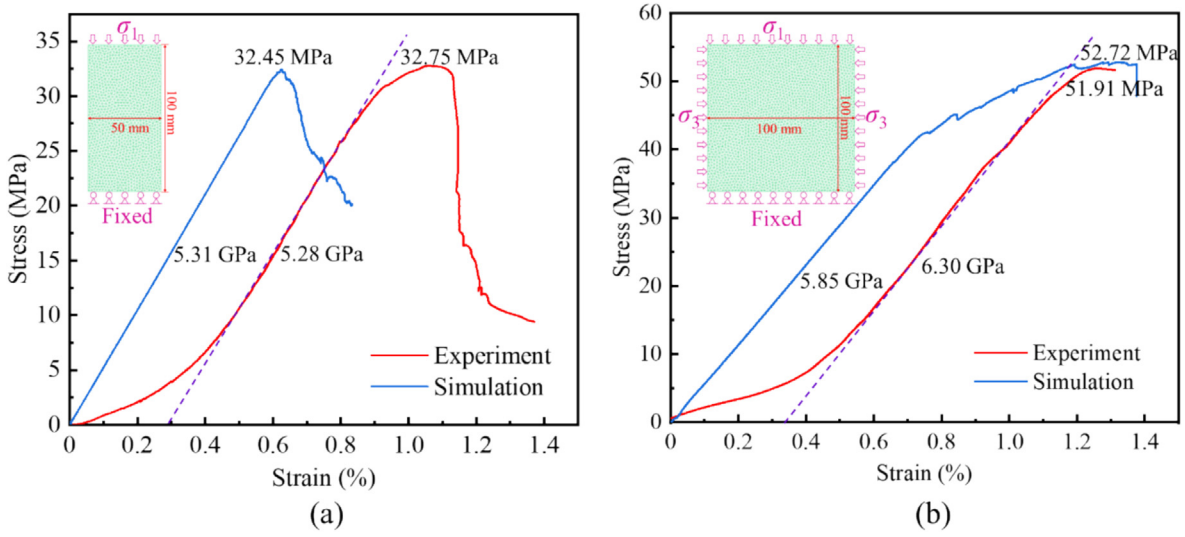

Fig. 14. Stress–strain curve verification. (a) Uniaxial compression, and (b) biaxial compression.

Table 5
Numerical simulation parameters.

Minerals	Block properties			Contact properties				
	Density (kg/m^3)	K (GPa)	G (GPa)	k_n (GPa/m)	k_s (GPa/m)	c (MPa)	φ (°)	σ_t (MPa)
Rock-like material	2200	4.9	3.1	44 789	17 916	9.0	34	2.1
Support material	7800	167	77	200 000	80 000	100	89	100
Joints	–	–	–	44 789	17 916	–	15	–

4.2 Stress evolution

Stress monitoring points were arranged around the arched hole and wedge blocks, as shown in Fig. 15. The evolution characteristics of tensile stress (σ_x) and shear stress (τ_{xy}) at each monitoring point were monitored during the stress loading process. "R" represents monitoring points at the midpoint of the arched hole roof, floor, and both sides, while "B" represents monitoring points at various locations along the boundary of the wedge block.

The evolution of tensile stress and shear stress before failure in the unsupported specimen was divided into three stages, and the strain percentage during each stage of the entire loading process was analyzed, as shown in Fig. 16. At monitoring point R_1 (as shown in Fig. 16(a)), during Stage I, the σ_x first increased and then decreased, while the τ_{xy} remained at a relatively low value. In Stage II, the σ_x and τ_{xy} of specimens "S1", "S2", and "S3" initially decreased and then increased. However, the σ_x and τ_{xy} of "S4" gradually decreased. In Stage III, the σ_x and τ_{xy} curves became approximately parallel, and the curves of specimens "S1" and "S2" overlapped. At monitoring point R_2 (as shown in Fig. 16(b)), in Stage I, the σ_x initially increased and then decreased, while the τ_{xy} remained relatively small. In Stage II, the values of σ_x and τ_{xy} were similar, exhibiting the same trend of variation. In Stage III, the curves of specimens "S2", "S3", and "S4" overlapped, while the curve of specimen "S1" remained approximately parallel. At monitoring point R_3 (as shown in Fig. 16(c)), in Stage I, both σ_x and τ_{xy} increased at a relatively slow rate, with the curves approximately overlapping. In Stage II, the rate of change for σ_x remained constant, while the rate of τ_{xy} increased. In Stage III, the τ_{xy} was much greater than the σ_x. At monitoring point R_4 (as shown in Fig. 16(d)), in Stage I, τ_{xy} increased at a high rate. In Stage II, the σ_x and τ_{xy} for specimens "S1" and "S2" changed at the same rate. In Stage III, the curves for "S1", "S2", and "S3" were parallel or overlapped, while for "S4", the rate of τ_{xy} increased. It can be concluded that, before the surrounding rock mass becomes unstable, the tunnel roof and floor initially experience relatively large σ_x, with the roof σ_x being greater than that of the floor. Subsequently, the σ_x decreases, and both σ_x and τ_{xy} ultimately tend to converge. The left side of the tunnel gradually bore larger τ_{xy}, reaching its maximum at the peak. The right side (wedge block sidewall) of the tunnel was influenced by different wedge blocks, and the trends of σ_x and τ_{xy} varied significantly.

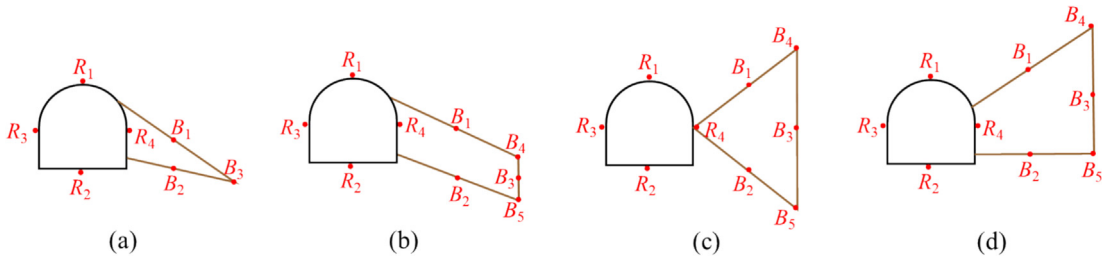

Fig. 15. Stress monitoring points at different locations of each specimen. (a) S1, (b) S2, (c) S3, and (d) S4.

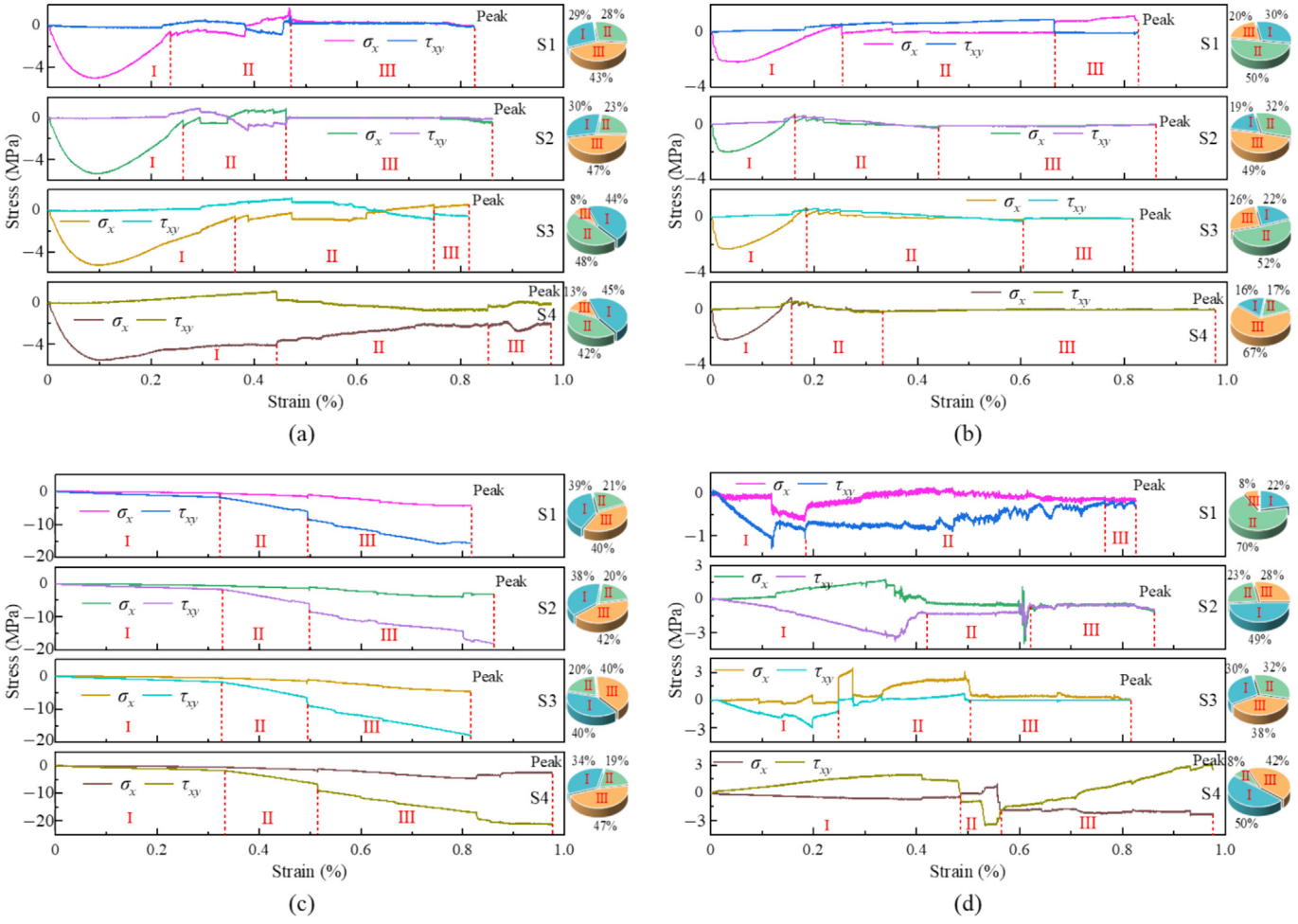

Fig. 16. Evolution of σ_x and τ_{xy} of unsupported specimen and strain percentage. (a) R_1, (b) R_2, (c) R_3, and (d) R_4.

The support system altered the evolution characteristics of σ_x and τ_{xy} in the original arched hole, as shown in Fig. 17. At monitoring point R_1 (Fig. 17(a)), the σ_x initially increased at a significant rate and then decreased, while the τ_{xy} gradually increased and then decreased. At monitoring point R_2 (Fig. 17(b)), the σ_x increased at a constant rate, reaching its maximum at the peak. At monitoring point R_3 (Fig. 17(c)), the σ_x first increased and then became approximately parallel to the τ_{xy}. Both the σ_x and τ_{xy} increased in the later stages, reaching their maximum values at the peak. At monitoring point R_4 (Fig. 17(d)), the σ_x of specimens "S1S" and "S2S" initially increased and then changed slightly, while the τ_{xy} first fluctuated slightly and then increased at the peak. For specimen "S3S", both the σ_x and τ_{xy} initially increased and then changed slightly. For specimen "S4S", the σ_x first increased, then decreased, and later increased in a stepwise manner, while the τ_{xy} increased stepwise at a relatively slow rate. After support,

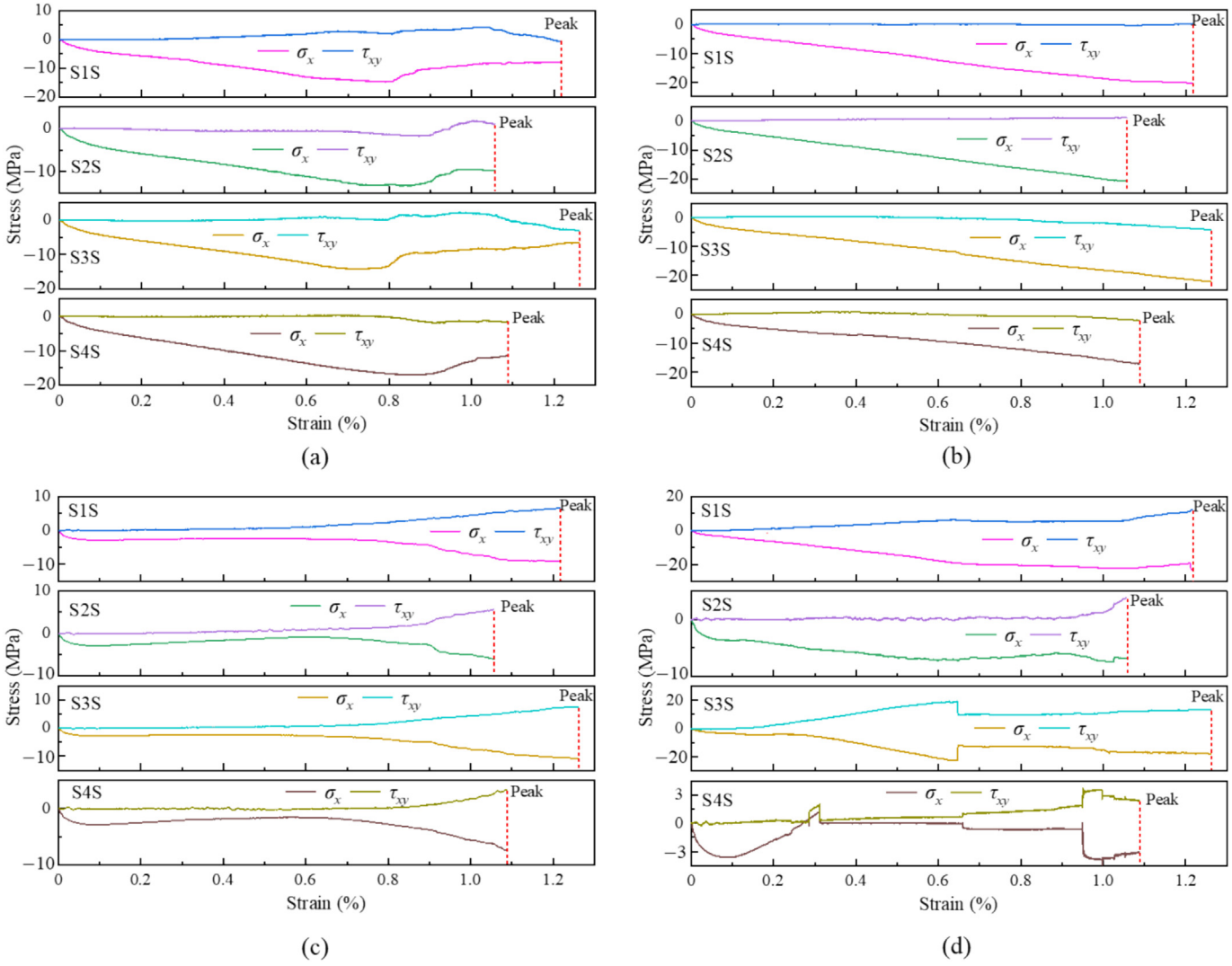

Fig. 17. Evolution curve of σ_x and τ_{xy} of the supported specimen. (a) R_1, (b) R_2, (c) R_3, and (d) R_4.

the σ_x in the tunnel surrounding rock generally increased, while the τ_{xy} on the left side decreased. The support had a significant differential effect on the σ_x and τ_{xy} of the right side, particularly for different types of wedge blocks.

4.3 Failure characteristics

After failure of the specimens, the influence characteristics of the wedge blocks on the stability of the hole and specimen are shown in Fig. 18. For the unsupported specimens, the area of the red high-displacement zone was smaller, while for the supported specimens, the area was larger. For the unsupported specimens, as shown in Fig. 18(a), in specimen "S1", spalling occurred on the right side of the arched hole, and shear slip took place at the upper interface of the wedge block, extending to the right boundary of the specimen. In specimen "S2", spalling occurred on the right side of the arched hole, with the maximum displacement observed on the surface of the wedge block. Shear slip was generated at the upper interface of the wedge block and extended along the vertex below the wedge block to the specimen boundary. In specimen "S3", no spalling occurred on the right side of the arched hole. Additionally, shear slip was observed at both the upper and lower interfaces of the wedge block, extending along the vertex below the wedge block to the specimen boundary. Tension failure occurred at the upper vertex of the wedge block. In specimen "S4", no spalling occurred on the right side of the arched hole. Shear slip took place at the upper interface of the block, and tension failure occurred at the upper vertex of the wedge block. Shear slip was also observed at the lower vertex of the wedge block, extending to the specimen boundary. For the supported specimens, as shown in Fig. 18(b), no spalling occurred within the arched hole, and the shear slip at the wedge block interfaces was controlled. In specimen "S1S", shear slip occurred at the upper interface of the wedge block, extending to the upper and lower boundaries of the speci-

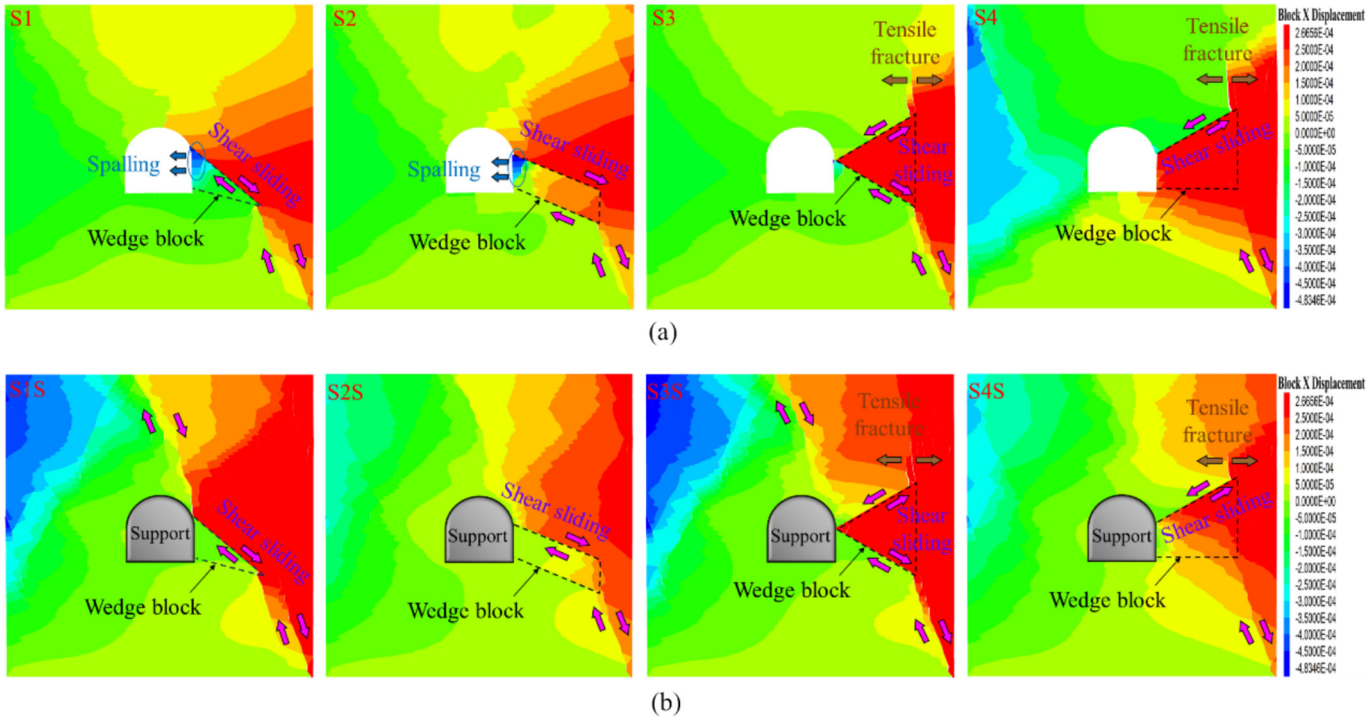

Fig. 18. Displacement cloud diagram after specimen failure. (a) Unsupported, and (b) supported.

men. In specimen "S2S", shear slip occurred at the upper interface of the wedge block, extending along the lower vertex of the wedge block to the lower boundary of the specimen. In specimen "S3S", shear slip occurred at both the upper and lower interfaces of the wedge block, extending to both the upper and lower boundaries of the specimen. Tension failure was observed at the upper vertex of the wedge block. In specimen "S4S", shear slip occurred at the upper interface of the wedge block, and shear slip at the lower vertex of the wedge block extended to the lower boundary of the specimen. Tension failure also occurred at the upper vertex of the wedge block. It can be concluded that, after the failure of unsupported specimens, significant damage occurred on the right side of the tunnel (wedge block sidewall), and the reduction in rock strength was primarily caused by instability due to the wedge block structure, which exhibited relatively high overall rock integrity. However, after failure in the supported specimens under high strength and high-stress conditions, the reduction in rock strength was mainly due to the instability caused by the rock material properties reaching their failure limit strength. The failure zones were larger, the fragmentation was more severe, and the rock integrity was poorer. The comparative analysis of failure under different working conditions is shown in Table 6. For the stable block specimens ("S1", "S2", "S1S", and "S2S"), only shear slip failure occurred. In contrast, for the extremely stable block specimens ("S3", "S4", "S3S", and "S4S"), both shear slip and tensile fracture failures were observed.

5 Discussion

5.1 Effect of horizontal stress

The geostress is linearly related to the burial depth (H), and the distribution of ground stress at various orientations corresponding to tunnel depth is shown in Fig. 19. The initial stress field of the underground rock mass is a three-dimensional compressive stress state ($\sigma_1 > \sigma_2 > \sigma_3$), with the maximum principal stress σ_1 in the vertical direction, the intermediate principal stress σ_2 and the minimum principal stress σ_3 in the horizontal direction (Du et al., 2015). In underground construction, the main tunnel is often excavated along the direction of the intermediate principal stress. Therefore, the stability of the tunnel is primarily controlled by σ_1 and σ_3, as shown in Fig. 19(a). However, previous studies have shown that various factors such as the horizontal stress acting on layered rock masses (Tian et al., 2023), jointed rock masses (Wang et al., 2021), surrounding rock properties(Bai & Wang, 2024), tunnel shape (Gong et al., 2019), and the relationship between the tunnel and stress orientations (Li et al., 2024; Du et al., 2024a) significantly affect tunnel stability. For tunnel surrounding rock with a wedge block, the stability of the sidewalls is primarily controlled by σ_3. In most underground mines, the three principal stresses increase with depth, as shown in Fig. 19(b). The σ_3 range corresponding to different depths of typical rock mass is calculated by $\sigma_3 = 0.0163H$, as shown in Table 7. Based on previous

Table 6
Comparative analysis of specimen failure under different working conditions.

Working conditions	Specimen No.	Wedge block type	Instability mode	Instability type	Failure characteristics
Unsupported	S1, S2	Stable	Shear slip	Structural instability	There is spalling on the side of the arched hole, and there are few or no high-displacement areas inside the wedge blocks.
	S3, S4	Extremely stable	Shear slip and tensile fracture		There is no spalling on the side of the arched hole, and there is a large high-displacement area inside the wedge block.
Supported	S1S, S2S	Stable	Shear slip	Material instability	There is no spalling on the side of the arch hole, the high displacement area inside the wedge block is small, and the high displacement area of the rock mass is large.
	S3S, S4S	Extremely stable	Shear slip and tensile fracture		There is no spalling on the side of the arch hole, there is a large high-displacement area inside the wedge block, and the high-displacement area of the rock mass is large.

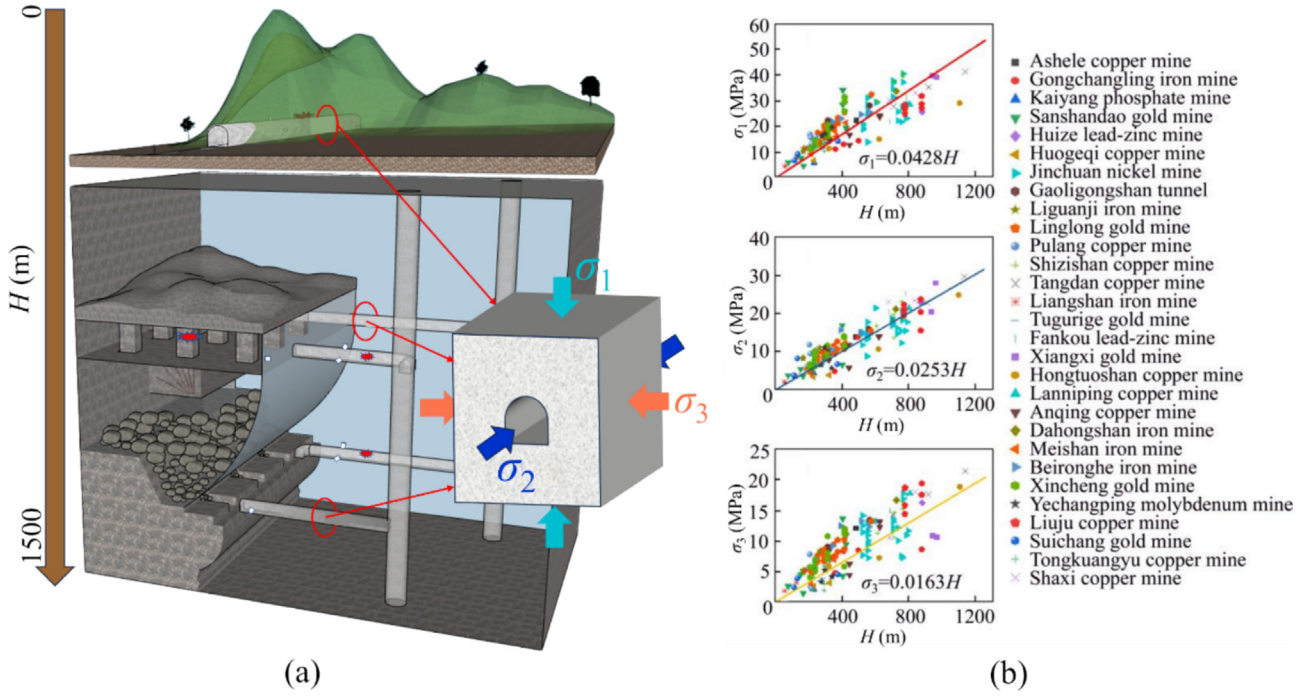

Fig. 19. Distribution of geostress corresponding to tunnel burial depth. (a) Tunnels with different burial depths, and (b) relationship between geostress and burial depth (Du et al., 2024b, 2020b).

studies at shallow depths, the horizontal stress σ_3 was set as 5, 10, 15, and 20 MPa for the study of horizontal stress at medium and deep depths.

Figure 20 shows the fitting line of σ_1 as a function of σ_3. The strength of the specimens increased with increasing horizontal stress. The slope of the fitting lines for specimens "S2" and "S4" was greater than that of "S1" and "S3". It can be concluded that, as the horizontal stress increased, the strength growth rate of quadrilateral wedge blocks was higher than that of triangular wedge blocks.

Figure 21 shows the failure characteristics of the right side of the tunnel under different horizontal stress states. As σ_3 was increased, the degree and extent of failure of the wedge block on the right side of the arched hole were found to have increased. As shown in Fig. 21(a) and (b), when $\sigma_3 = 5$ MPa, the surface of the wedge block in specimens "S1" and "S2" experienced failure. As the horizontal stress increased, the failure gradually transferred deeper into the wedge block. When $\sigma_3 = 20$ MPa, the wedge block in specimen "S1" experienced large-scale slab cracking,

Table 7
Horizontal stress values corresponding to the burial depth under typical conditions.

H (m)	σ_3 (MPa)	Value (MPa)	Rock mass characteristics
100–300	1.63–4.89	3	Sandstone, shale, shallow loose or low-density rock, many joints and fissures, low-stress areas, shallow tunnels, and initial mining development.
300–500	4.89–8.15	5	Medium-density rock mass, such as sandstone and limestone, with fewer joints and better rock integrity, medium-deep mining, and underground energy storage design.
500–800	8.15–13.04	10	Limestone, shale, hard sandstone, etc., dense rock mass, rock burst risk, deep coal mines, and underground gas storage.
800–1000	13.04–16.3	15	Quartz sandstone, granite, and other hard rocks, highly dense rock mass, high stress concentration, deep energy development, and geothermal good construction.
1000–1500	16.3–24.45	20	Hard rocks such as granite and basalt have high rock density, high-level stress concentration, and significant risk of rock bursts, such as ultra-deep mining and ultra-deep geothermal drilling.

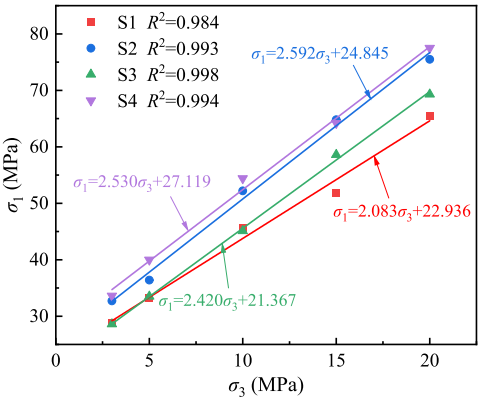

Fig. 20. Fitting line of σ_1 changing with σ_3.

with the failure spreading inward toward the arched hole. In contrast, in specimen "S2", the shallow part of the wedge block experienced failure and spalled off. As shown in Fig. 21(c) and (d), when $\sigma_3 = 5$ MPa, the surface of the right-side surrounding rock of the arched hole in specimens "S3" and "S4" experienced failure. As the horizontal stress increased, the extent of the failure gradually expanded. When $\sigma_3 = 20$ MPa, both the wedge block and the surrounding rock on the right side of the arched hole in specimens "S3" and "S4" failed and spalled off. The presence of the wedge block led to varying degrees of damage to the surrounding rock of the arched hole. Specimen "S1" exhibited the most extensive and severe failure, while specimen "S3" exhibited the least. It can be concluded that the triangular wedge blocks play a decisive role in the stability of the tunnel surrounding rock. Specifically, the safety of the stable triangular blocks contained in specimen "S1" is the lowest, while the extremely stable triangular blocks in specimen "S3" are the highest. As the number of wedge block sides increased, the damage to the stable wedge block decreased, while the damage to the extremely stable wedge block increased.

5.2 Effect of multiple joints

Taking the extremely stable wedge blocks as an example, when the number of joints is four or more, the rock mass is divided by joints into either single or multiple discrete blocks, as shown in Fig. 22. In Fig. 22(a), the wedge-surrounding rock interaction mechanism established in this study still applies when the polytope is cut into a polygonal block. In Fig. 22(b), when multiple joints are cut into multiple blocks, the surrounding rock shows the characteristics of a multi-body discontinuous structure, and the damage mode may shift from slip to random block combination instability. Preliminary analysis shows that with the increase in the number of joints, the surrounding rock damage presents three significant characteristics: (1) the stress redistribution extends from the periphery of the local wedge block to a wider range; (2) the energy release mode changes from centralized and sudden to multi-stage cumulative; and (3) the support system needs to be changed from passive load-bearing to active stress regulation. Further research should focus on cross-scale investigations of surrounding rock failure under multi-joint conditions, aiming to fill the gaps regarding the progressive failure mechanisms of block assemblages and their support control strategies.

6 Conclusions

This study investigated the mechanical mechanisms of interaction between different wedge blocks and surrounding rock, as well as their impact on the stability of tunnel sidewalls. A typical stability analysis method for wedge blocks was proposed. By combining experimental and numerical simulation methods, the stress evolution patterns of wedge blocks and arched tunnel features during loading, and their influence on the surrounding rock instability mechanisms were revealed. The results indicated that, compared to unsupported specimens, supported specimens exhibited higher strength and stability in both the peak and post-peak stages. Notably, in the post-peak stage, the strength of the supported specimens decreased more slowly, and the crack propagation process was relatively smoother. Support had a significant impact on the energy storage and release processes, with supported specimens demonstrating higher energy storage capacity at the peak. Support also made the stress variation patterns in each

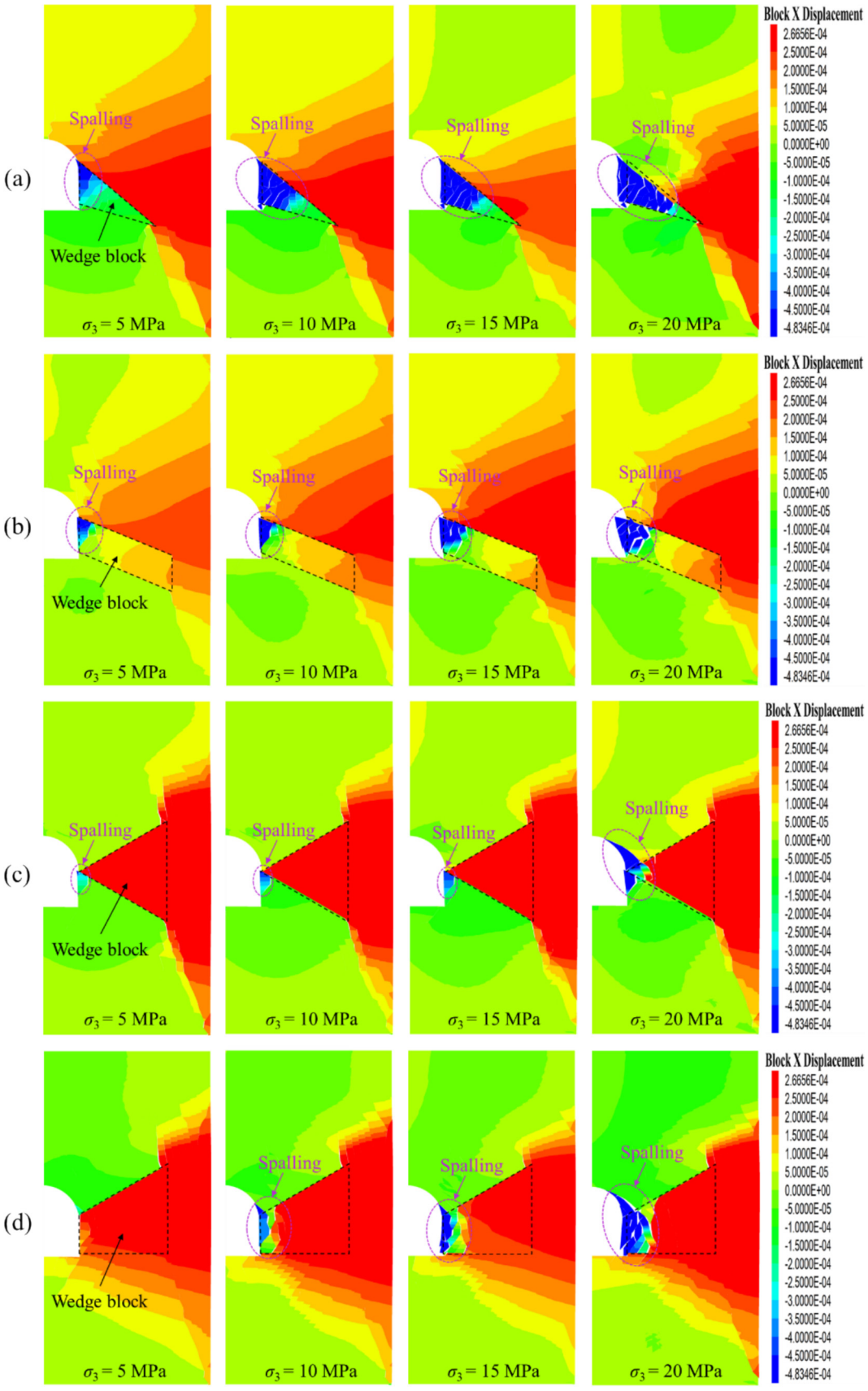

Fig. 21. Failure characteristics of the right side of the arched hole under different horizontal stresses. (a) S1, (b) S2, (c) S3, and (d) S4.

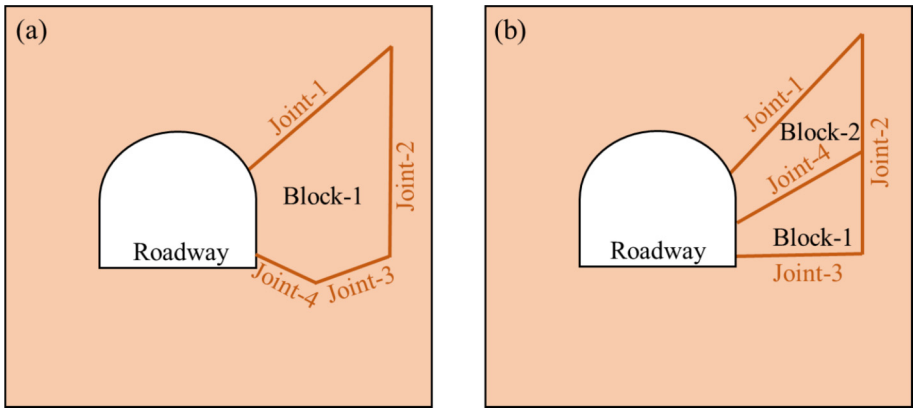

Fig. 22. Schematic diagram of a multi-jointed cutting block. (a) Single block, and (b) multiple blocks.

stage more distinct. In terms of failure modes, stable specimens only experienced shear slip failure, while extremely stable specimens underwent both shear slip and tensile fracture failures. As the minimum principal stress (σ_3) increased, the degree of wedge block failure and the strength of the specimens both increased. The triangular wedge blocks played a critical role in the stability of the tunnel surrounding rock.

The support measures significantly improved the stability of the surrounding rock by regulating the stress distribution and the crack propagation process. In the supported specimens, both the tensile stress (σ_x) and shear stress (τ_{xy}) showed considerable changes, particularly near the wedge block, where the stress state was notably altered. The support helped redistribute the stress concentration areas, thereby suppressing rock mass instability. Support effectively enhanced the energy storage capacity of the surrounding rock and changed the stress state near different types of wedge blocks, influencing the stress evolution process. The stable triangular blocks exhibited lower safety, whereas extremely stable triangular blocks demonstrated stronger stability. The shape and stability of the wedge block directly affect the stability of the tunnel surrounding rock. The results of the study have revealed the mechanical behavior and progressive instability characteristics of the wedge block structure in the roadway sidewall, which provides a theoretical basis for the stability control of the jointed surrounding rock and the early warning of disasters.

Data availability

The data that support the findings of this study are available from the corresponding author upon reasonable request.

CRediT authorship contribution statement

Ruiyang Bi: Formal analysis, Writing – original draft, Conceptualization. **Minghui Liu:** Validation, Investigation. **Jian Zhou:** Investigation. **Kun Du:** Conceptualization, Funding acquisition, Resources.

Declaration of competing interest

The authors declare that they have no known competing financial interests or personal relationships that could have appeared to influence the work reported in this paper.

Acknowledgement

The authors would like to thank the National Natural Science Foundation of China (Grant No. 52374150), the Key Science and Technology Program of the Ministry of Emergency Management of the People's Republic of China (2024EMST141405), and the Innovation-Driven Project of Central South University (No. 2023ZZTS0714).

References

Bai, X. Y., & Wang, X. B. (2024). Simulation of cracking processes of the rectangular cavern surrounding rock based on a continuum-discontinuum method. *Engineering Fracture Mechanics, 307*, 110304.

Bi, R. Y., Liu, M. H., Li, G. C., Zhou, J., & Du, K. (2024). Mechanical properties and risk characterization of surrounding rocks containing various blocks of arch-shaped holes under biaxial compression. *Engineering Failure Analysis, 158*, 107983.

Du, K., Niu, T. F., Sun, Y., Zhou, J., Liu, J., Wang, S. F., & Liu, K. (2024a). Crack evolution and failure mechanisms of rock specimens with oblique cylindrical holes in biaxial compression tests. *Rock Mechanics and Rock Engineering, 57*(5), 3257–3280.

Du, K., Bi, R. Y., Khandelwal, M., Li, G. C., & Zhou, J. (2024b). Occurrence mechanism and prevention technology of rockburst, coal bump and mine earthquake in deep mining. *Geomechanics and Geophysics for Geo-Energy and Geo-Resources, 10*(1), 98.

Du, K., Li, X. B., Li, D. Y., & Weng, L. (2015). Failure properties of rocks in true triaxial unloading compressive test. *Transactions of Nonferrous Metals Society of China, 25*(2), 571–581.

Du, K., Li, X. F., Tao, M., & Wang, S. F. (2020a). Experimental study on acoustic emission (AE) characteristics and crack classification during rock fracture in several basic lab tests. *International Journal of Rock Mechanics and Mining Sciences, 133*, 104411.

Du, K., Li, X. F., Yang, C. Z., Zhou, J., Chen, S. J., & Khandelwal, M. (2020b). Experimental investigations on mechanical performance of rocks under fatigue loads and biaxial confinements. *Journal of Central South University, 27*(10), 2985–2998.

Fan, H. Y., Li, L. P., Zong, P. J., Liu, H. L., Yang, L. J., Wang, J., Yan, P., & Sun, S. Q. (2023). Advanced stability analysis method for the tunnel face in jointed rock mass based on DFN-DEM. *Underground Space, 13*, 136–149.

Fan, L. F., Wang, L. J., Wang, M., & Wu, Z. J. (2020). Investigation of stress wave transmission across a nonlinearly jointed complex rock mass. *International Journal of Rock Mechanics and Mining Sciences, 136*, 104485.

Feng, X. T., Pei, S. F., Jiang, Q., Zhou, Y. Y., Li, S. J., & Yao, Z. B. (2017). Deep fracturing of the hard rock surrounding a large underground cavern subjected to high geostress: In situ observation and mechanism analysis. *Rock Mechanics and Rock Engineering, 50*(8), 2155–2175.

Feng, X. T., Xu, H., Qiu, S. L., Li, S. J., Yang, C. X., Guo, H. S., Cheng, Y., & Gao, Y. H. (2018). In situ observation of rock spalling in the deep tunnels of the China Jinping underground laboratory (2400 m Depth). *Rock Mechanics and Rock Engineering, 51*(4), 1193–1213.

Fraldi, M., Cavuoto, R., Cutolo, A., & Guarracino, F. (2019). Stability of tunnels according to depth and variability of rock mass parameters. *International Journal of Rock Mechanics and Mining Sciences, 119*, 222–229.

Gong, F. Q., Wu, W. X., Li, T. B., & Si, X. F. (2019). Experimental simulation and investigation of spalling failure of rectangular tunnel under different three-dimensional stress states. *International Journal of Rock Mechanics and Mining Sciences, 122*, 104081.

Hu, J., Pan, H. L., Liu, H. L., Li, L. P., Fan, H. Y., & Liu, Q. C. (2023). Response of acoustic emission and vibration monitoring data during rock block collapse in the tunnel: Small- and large-scale experiments study. *Tunnelling and Underground Space Technology, 137*, 105121.

Ji, P. X., Viegas, G., & Zhang, Q. B. (2024). Mechanical and fracturing characteristics of defected rock-like materials under biaxial compression. *International Journal of Rock Mechanics and Mining Sciences, 176*, 105692.

Jiang, F., Wang, G., He, P., Hou, B., Zhang, S. B., Sun, S. Q., Zheng, C. C., & Wu, Y. (2022). Mechanical failure analysis during direct shear of double-joint rock mass. *Bulletin of Engineering Geology and the Environment, 81*(10), 410.

Li, X. F., Du, K., Zhou, J., & Yin, Z. Q. (2024). Failure behaviors of square-tunnel-structured rock specimens under various inclined boundary stress conditions. *Engineering Failure Analysis, 157*, 107888.

Li, X. B., Gong, F. Q., Tao, M., Dong, L. J., Du, K., Ma, C. D., Zhou, Z. L., & Yin, T. B. (2017). Failure mechanism and coupled static-dynamic loading theory in deep hard rock mining: A review. *Journal of Rock Mechanics and Geotechnical Engineering, 9*(4), 767–782.

Liu, B. L., Li, B., Zhang, L., Huang, R., Gao, H. C., Luo, S. L., & Wang, T. (2024a). Disc-cutter induced rock breakage mechanism for TBM excavation in rock masses with different joint shear strengths. *Underground Space, 19*, 119–137.

Liu, M. H., Bi, R. Y., Luo, X. Y., & Du, K. (2024b). Natural joint effect on mechanical characteristics and fracture evolution of in-situ rocks under uniaxial compression. *Engineering Failure Analysis, 157*, 107880.

Liu, X. F., Pan, P. Z., Zhou, Y. Y., Wang, Z. F., & Xu, D. P. (2024c). Role of foliation occurrence and stress orientation on asymmetric failure in foliated rock tunnel: Insight from numerical simulation. *Engineering Failure Analysis, 160*, 108174.

Liu, X. H., Zhang, K., Liu, W. L., & Xie, J. B. (2022). Influence of weak inclusions on the cracking behavior of a jointed rock mass containing an opening: Insights from DIC-based approaches. *Archives of Civil and Mechanical Engineering, 22*(4), 184.

Shi, L., Li, C. C., & Zhang, X. W. (2024). Laboratory tests of strain burst in boreholes of four types of rocks under biaxial loading. *Rock Mechanics and Rock Engineering, 58*(1), 301–319.

Tian, Y., Shu, X. Y., Tian, H. M., He, L. K., Jin, Y., & Huang, M. (2023). Effect of horizontal stress on the mesoscopic deformation and failure mechanism of layered surrounding rock masses in tunnels. *Engineering Failure Analysis, 148*, 107226.

Wang, H. B., Wang, F. M., Guo, C. C., Qin, L., Liu, J., & Qu, T. M. (2025). Experimental investigation on the failure characteristic and synergistic load-bearing mechanism of multi-layer linings for deep soft rock tunnels. *Underground Space, 20*, 259–276.

Wang, X. S., Iura, T., Jiang, Y. J., Wang, Z. Q., & Liu, R. C. (2021). Deformation and mechanical characteristics of tunneling in squeezing ground: A case study of the west section of the Tawarazaka Tunnel in Japan. *Tunnelling and Underground Space Technology, 109*, 103697.

Wu, W. X., Gong, F. Q., & Zhang, Z. X. (2024). Experimental investigation on rockburst characteristics of highly stressed D-shape tunnel subjected to impact load. *Underground Space, 19*, 153–168.

Wu, W., Zhu, H. H., Lin, J. S., Zhuang, X. Y., & Ma, G. W. (2018). Tunnel stability assessment by 3D DDA-key block analysis. *Tunnelling and Underground Space Technology, 71*, 210–214.

Yang, G. Y., Li, L. P., Liu, H. L., Lai, Y. B., Zhu, C., Hou, J., & Dai, Y. H. (2023). Experimental study on evolution law of dynamic characteristic parameters during the tunnel surrounding rock block collapse process. *Tunnelling and Underground Space Technology, 140*, 105336.

Yang, Z., Tao, M., Fei, W. B., Yin, T. B., Gu, X. Y., & Narsilio, G. A. (2024). A coupled thermo-mechanical model for investigating cracking and failure of composite interbedded rock. *Engineering Geology, 339*, 107645.

Zhang, J. Z., & Zhou, X. P. (2020). Forecasting catastrophic rupture in brittle rocks using precursory AE time series. *Journal of Geophysical Research: Solid Earth, 125*(8), e2019JB019276.

Zhang, K., Guan, S. H., Liu, X. H., Yao, C. X., Yan, L., & Fan, W. C. (2023). Macro- and micromechanical properties of flawed sandstone and their degradation mechanisms under hydrodynamic scouring. *Engineering Fracture Mechanics, 292*, 109665.

Zhang, W., Qiu, Z., Liu, W. R., Zhang, B. L., & Guo, W. Y. (2024a). Study on the AE characteristics and energy evolution mechanism of sandstone with different aspect ratios under biaxial compression. *Rock Mechanics and Rock Engineering, 57*(11), 9019–9034.

Zhang, X., Yang, Y., Yang, R. S., Li, J., Chen, S. L., & Li, D. (2024b). Study on dynamic mechanical characteristics of specimens with cavity under prestressing conditions. *Engineering Fracture Mechanics, 312*, 110602.

Zhao, F., Shi, Z. M., Yu, S. B., & Zheng, H. C. (2023a). A review of fracture mechanic behaviors of rocks containing various defects. *Underground Space, 12*, 102–115.

Zhao, Z. H., Sun, W., Chen, S. J., & Liu, H. (2023b). Shear behaviour of anchored jointed rock mass under different engineering conditions considering damage and joint surface morphology. *Underground Space, 13*, 316–334.

Zhu, H. H., Wu, W., Chen, J. Q., Ma, G. W., Liu, X. G., & Zhuang, X. Y. (2016). Integration of three dimensional discontinuous deformation analysis (DDA) with binocular photogrammetry for stability analysis of tunnels in blocky rockmass. *Tunnelling and Underground Space Technology, 51*, 30–40.

Zhu, J. B., Ren, M., & Liao, Z. Y. (2020). Wave propagation and diffraction through non-persistent rock joints: An analytical and numerical study. *International Journal of Rock Mechanics and Mining Sciences, 132*, 104362.